

Old Dominion University Research Foundation

DNA/LANGLEY
P.90

DEPARTMENT OF MECHANICAL ENGINEERING AND MECHANICS
COLLEGE OF ENGINEERING AND TECHNOLOGY
OLD DOMINION UNIVERSITY
NORFOLK, VIRGINIA 23508

IN-52

69604 CL

INVESTIGATION OF CHEMICALLY REACTING AND RADIATING SUPERSONIC INTERNAL FLOWS

By

M. Mani, Graduate Research Assistant

and

S. N. Tiwari, Principal Investigator

Progress Report

For the period ended August 31, 1986

Prepared for the
National Aeronautics and Space Administration
Langley Research Center
Hampton, Virginia 23665

Under

Research Grant NAG-1-423

Dr. A. Kumar and J. P. Drummond, Technical Monitors
HSAD-Computational Methods Branch

N87-25994

(NASA-CR-180540) INVESTIGATION OF
CHEMICALLY REACTING AND RADIATING SUPERSONIC
INTERNAL FLOWS Progress Report, period
ending 31 Aug. 1986 (Old Dominion Univ.) Unclassified
70 p Avail: NTIS HC A04/MF A01 CSCL 01A G3/02 0069604

December 1986

DEPARTMENT OF MECHANICAL ENGINEERING AND MECHANICS
COLLEGE OF ENGINEERING AND TECHNOLOGY
OLD DOMINION UNIVERSITY
NORFOLK, VIRGINIA 23508

INVESTIGATION OF CHEMICALLY REACTING AND
RADIATING SUPERSONIC INTERNAL FLOWS

By

M. Mani, Graduate Research Assistant

and

S. N. Tiwari, Principal Investigator

Progress Report
For the period ended August 31, 1986

Prepared for the
National Aeronautics and Space Administration
Langley Research Center
Hampton, Virginia 23665

Under

Research Grant NAG-1-423

Dr. A. Kumar and J. P. Drummond, Technical Monitors
HSAD-Computational Methods Branch

Submitted by the
Old Dominion University Research Foundation
P.O. Box 6369
Norfolk, Virginia 23508



December 1986

FOREWORD

This is a progress report on the research project "Analysis and Computation of an Internal Flow Field in a Scramjet Engine," for the period ended August 31, 1986. The work was supported by the NASA/Langley Research Center (Computational Methods Branch of the High-Speed Aerodynamics Division) through research grant NAG-1-423. The grant was monitored by Dr. Ajay Kumar and Mr. J. Philip Drummond of the High-Speed Aerodynamics Branch.

INVESTIGATION OF CHEMICALLY REACTING
AND RADIATING SUPERSONIC INTERNAL FLOWS

M. Mani* and S. N. Tiwari†

ABSTRACT

The two-dimensional spatially elliptic Navier-Stokes equations are used to investigate the chemically reacting and radiating supersonic flow of the hydrogen-air system between two parallel plates and in a channel with a ten-degree compression-expansion ramp at the lower boundary. The explicit unsplit finite-difference technique of MacCormack is used to advance the governing equations in time until convergence is achieved. The chemistry source term in the species equation is treated implicitly to alleviate the stiffness associated with fast reactions. The tangent slab approximation is employed in the radiative flux formulation. Both pseudo-gray and nongray models are used to represent the absorption-emission characteristics of the participating species. Results obtained for specific conditions indicate that the radiative interaction can have a significant influence on the flow field.

*Graduate Research Assistant, Department of Mechanical Engineering and Mechanics, Old Dominion University, Norfolk, Virginia 23508.

†Eminent Professor, Department of Mechanical Engineering and Mechanics, Old Dominion University, Norfolk, Virginia 23508.

TABLE OF CONTENTS

	<u>Page</u>
LIST OF TABLES	v
LIST OF FIGURES	v
NOMENCLATURE	vi
1. INTRODUCTION	1
2. GENERAL FORMULATION	2
2.1 Physical System and Model	2
2.2 Basic Governing Equations	5
2.3 Chemistry Model	8
2.4 Thermodynamics Model	11
3. RADIATION TRANSPORT MODEL	14
3.1 Radiation Absorption Models	14
3.1.1 Gray Gas Model	14
3.1.2 Nongray Gas Model	15
3.2 Radiative Flux Equations	17
3.2.1 Basic Formulation	18
3.2.2 Gray Formulation	20
3.2.3 Nongray Formulation	22
4. METHOD OF SOLUTION	25
4.1 Grid Generation	25
4.2 Solution of the Governing Equations	28
5. RESULTS AND DISCUSSION	30
6. CONCLUSION	51
REFERENCES	52
APPENDIX A: DERIVATION OF CONDUCTION HEAT FLUX TERMS	56
APPENDIX B: DERIVATION OF RADIATIVE HEAT FLUX TERM	58
APPENDIX C: DERIVATION OF THE BOUNDARY CONDITION FOR GRAY GAS MODEL	61

LIST OF TABLES

<u>Table</u>		<u>Page</u>
2.1	Numerical Values of Various Constants	13

LIST OF FIGURES

<u>Figure</u>		<u>Page</u>
2.1	Propulsion alternatives	4
2.2	Airframe - integrated supersonic combustion ramjet	4
2.3	Flow field near an injector	6
4.1	Grid structure	27
5.1	Plane radiating layer between parallel boundaries	35
5.2	Radiating flow in a channel with compression-expansion ramp	36
5.3	Radiative flux along the channel for 50% H ₂ O	37
5.4	Radiative flux vs. y at the channel exit	38
5.5	Radiative flux vs. y at x=5 and 10 cm	39
5.6	Radiative and conductive flux vs. y at x=5 and 10 cm	40
5.7	Comparison of results for gray and nongray radiation	41
5.8	Pressure contours for nonreaching flow in a channel with a ramp	42
5.9	Radiative flux vs. x for two different free-stream velocities	43
5.10	Radiative flux vs. x for two different gas compositions	44
5.11	Pressure contours for reacting flow in a channel with a ramp	45
5.12	Mass fraction vs. x at the lower boundary	46
5.13	Mass fraction vs. x at y=1.5 cm	47
5.14	Radiative flux vs. x for reacting and nonreacting flows	48
5.15	Temperature vs. x for reacting and radiating flows	49
5.16	Mass fraction vs. x for reacting and radiating flows	50

NOMENCLATURE

A	band absorptance
A_0	band width parameter
C_j	concentration of the jth species
C_o	correlation parameter
C_p	constant pressure specific heat
e_ω	Planck's function
E	total internal energy
f_j	mass fraction of the jth species
h	static enthalpy of mixture
H	total enthalpy
I	identity matrix
k	thermal conductivity
K_b	backward rate constant
K_f	forward rate constant
M_j	molecular weight of the jth species
P	pressure
P_j	partial pressure of the jth species
P_e	equivalent broadening pressure ratio
Pr	Prandtl number
q_R	total radiative heat flux
$q_{R\omega}$	spectral radiative heat flux
S	integrated band intensity
T	temperature
u,v	velocity in x and y direction
\dot{w}_j	production rate of the jth species
x,y	physical coordinate
z	dummy variable in the y direction
γ	ratio of specific heats
Δt_{ch}	chemistry time step
Δt_f	fluid-dynamic time step
κ	absorption coefficient
$\kappa_\lambda, \kappa_\omega$	spectral absorption coefficient
κ_p	Planck mean absorption coefficient

λ	second coefficient of viscosity, wave length
μ	dynamic viscosity (laminar flow)
ξ, η	computational coordinates
ρ	density
σ	Stefan-Boltzmann constant
ϕ	equivalence ratio
ω	wave number

1. INTRODUCTION

In the last several years there has been a great deal of research toward development of a hypersonic transatmospheric vehicle. At the NASA Langley Research Center the hydrogen-fueled scramjet (supersonic combustion ramjet) engine has been a strong candidate for propelling such a vehicle. For a better understanding of the complex flow field in different regions of the engine, both experimental and computational techniques are being employed. Several computer programs [1-4]* have been developed to gain more insight into the problem involving the flow in the various sections of the scramjet module.

The purpose of this study is to investigate the effect of radiative heat transfer in chemically reacting supersonic flow in the scramjet combustor. The combustion of hydrogen and air results in absorbing-emitting gases such as water vapor and hydroxyl radical. The presence of such gases makes the study of radiative heat transfer in chemically reacting flows an important issue.

There are several models available in the literature to represent the absorption-emission characteristics of molecular gases [5-11]. Some specific applications of the models to flow and combustion related problems are available in [8, 9, 12-14]. Both gray and nongray gas models are used in this study. The gray gas model is less accurate but is much more efficient for parametric studies. For this model, the radiative heat flux is independent of the wavelength and the governing equations can be expressed in terms of second order nonhomogenous ordinary differential equations (ODE). This system of ODE's forms a tridiagonal matrix which is solved by the Thomas algorithm.

The flow field in the combustor is represented by the Navier-Stokes

*The numbers in brackets indicate references.

equations and the appropriate number of species continuity equations [1-4]. Incorporation of the finite rate chemistry model into the fluid dynamic equations creates a set of stiff differential equations. The stiffness is due to a disparity in the time scales of the governing equations. In the time accurate solution after the fast transients have decayed and the solutions are changing slowly, taking a larger time step is necessary for efficiency purposes. But explicit methods still require small time steps to maintain stability. An eigenvalue problem associated with stiff ODE has been solved to express this point clearly in [2]. One way around this problem is to use a fully implicit methods. This method, however, requires the inversion of a block multi-diagonal system of algebraic equations. This is difficult to implement to take full advantage of vector processing computers such as VPS-32. The use of a semi-implicit technique, suggested by several investigators [15-17], provides an alternative to the above problems. This technique treats the source term (which is the cause of the stiffness) implicitly, and solves the rest of equations explicitly.

2. GENERAL FORMULATION

A brief discussion is presented on various components of the scramjet engine. Special attention is directed in discussion of the basic equations that are applicable in analyzing the flow field in different parts of the engine. The relations for the thermodynamic and chemistry models are also provided in this section.

2.1 Physical System and Model

As mentioned in the introduction, the scramjet engine has been a candidate for propelling the hypersonic vehicle. In Fig. 2.1, various air breathing and rocket propulsion alternatives are shown [18, 19]. For Mach

numbers zero to three turbojet air breathing systems have the highest performance. Above Mach number of three, turbine inlet temperatures constrain performance, and then the ramjet becomes more attractive. At about Mach number of six, the performance of the ramjet is greatly reduced. This is due to dissociation of the reaction product which is caused by slowing the supersonic flow to subsonic flow. Therefore, it is more efficient to allow the engine internal flow to remain at supersonic speed. Thus for Mach number of six and beyond, the fixed geometry scramjet is clearly superior for propelling a vehicle at hypersonic speed. Hydrogen has been selected as the fuel for the scramjet due to its capability of cooling the engine and the airframe and also because of its high impulse level.

The scramjet engine is made up of several identical modules and it is installed underneath the aircraft as shown in Fig. 2.2. As part of the engine design concept, the forebody of the aircraft acts as an inlet (airframe integrated [19]) for precompression and the afterbody as a nozzle for post expansion. Since the vehicle compresses the airflow in the vertical direction, the module size walls are made wedge shaped to compress the flow horizontally. This tends to minimize the flow distortion. The diamond shape strut is located at the minimum cross sectional area to complete the compression and it also provides the fuel injection. Each module is made up of inlet, combustor and nozzle regions.

The inlet region starts with the forebody of the vehicle and ends up with the minimum cross sectional area of each module. In the first part, the air flow is compressed by the oblique shock generated from the forebody before it enters the engine. For numerical solution, the flow is best represented by the Navier-Stokes equation in the actual inlet area of the engine. Using the Euler equation away from the wall and the boundary layer equation near the

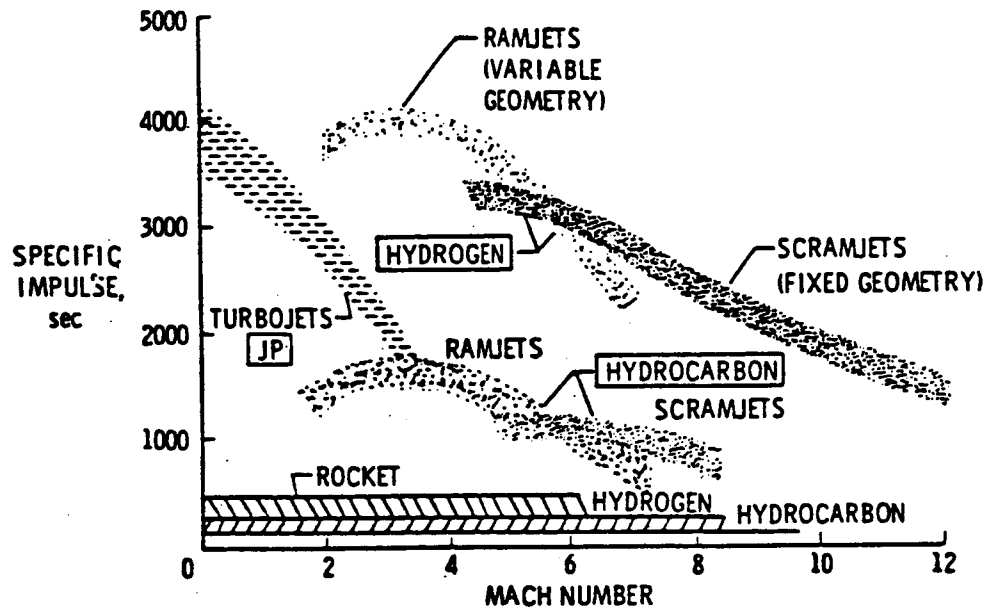


Fig. 2.1 Propulsion alternatives.

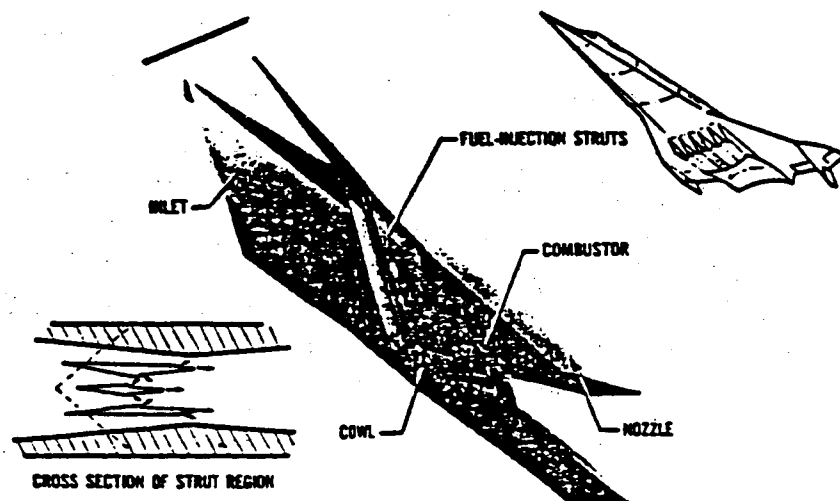


Fig. 2.2 Airframe-integrated supersonic combustion ramjet.

wall region can be complicated by the oblique shock interaction with the boundary layer. This can cause the flow separation which means flow can not be represented accurately by these equations. The chemistry is frozen in this region ($\tau_{ch.} \gg \tau_{f1.}$). Three-dimensional Navier-Stokes equations have been employed by Kumar [3] to investigate the flow field in this region with a reasonable success. Chitsomboon et al. [4] have employed the parabolized Navier-Stokes equations with limited success.

The combustor region is by far the most complex part of the scramjet engine. As a result, a great deal of research is directed toward better understanding of the combustor flow field. The flow in this region is usually supersonic but it can be both supersonic and subsonic (Fig. 2.3). The fluid dynamics becomes complicated by the fuel injection, flame holding, chemistry, radiation and turbulence. The flow field in this region is represented by the elliptic Navier-Stokes (including turbulence, chemistry and radiation) equations. In the farfield (downstream of the fuel injection strut where the flow is only supersonic) the flow can be represented by the parabolized Navier-Stokes equations [4].

The nozzle and subsurface of the afterbody provide about fifty percent of the thrust at Mach number six [19]. The flow through the nozzle is supersonic and the chemistry is frozen. However the combustor exit flow consists of multicomponents of the reacting species, multiple shock, and 3-D viscous effects. The flow can be represented by the parabolized Navier-Stokes equations.

2.2 Basic Governing Equations

The two-dimensional Navier-Stokes and species continuity equations are represented in physical domain by

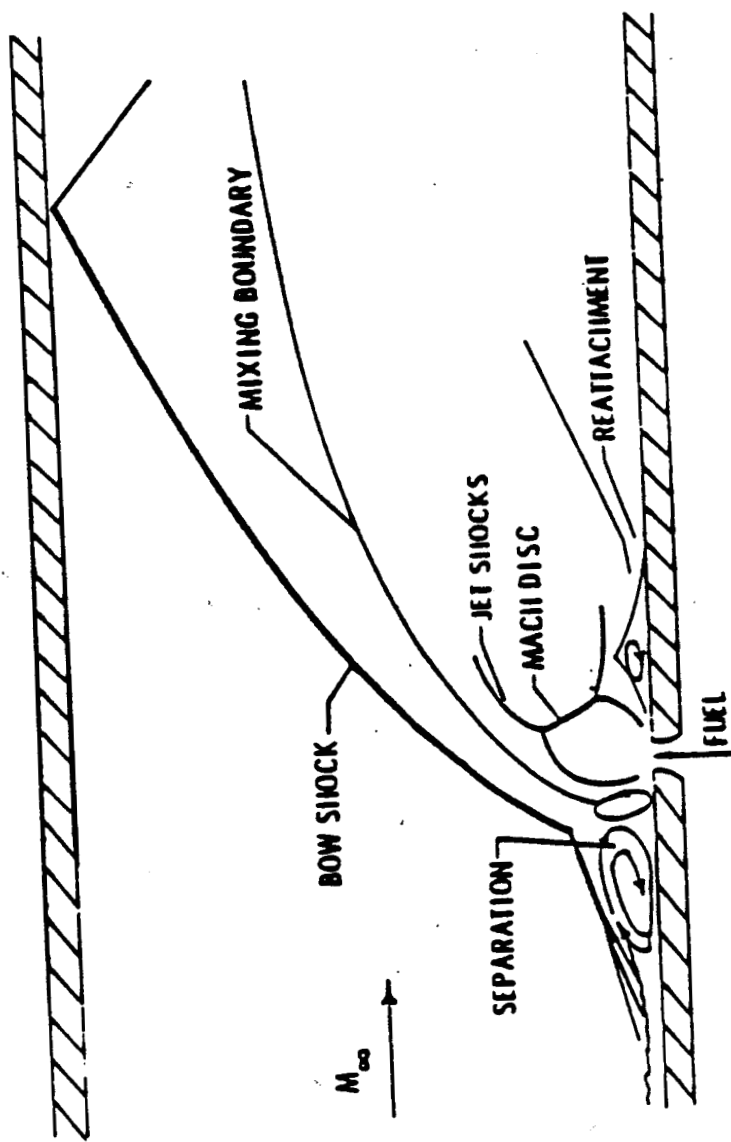


Fig. 2.3 Flow field near an injector.

$$\frac{\partial U}{\partial t} + \frac{\partial F}{\partial x} + \frac{\partial G}{\partial y} + H = 0 \quad (2.1)$$

where vectors U , F , G and H are expressed as

$$U = \begin{bmatrix} \rho \\ \rho u \\ \rho v \\ \rho E \\ \rho f_j \end{bmatrix} \quad F = \begin{bmatrix} \rho u \\ \rho u^2 + \tau_{xx} \\ \rho uv + \tau_{xy} \\ (\rho E + \tau_{xx}) u + \tau_{xy} v + q_{cx} \\ \rho u f_j - \rho D \frac{\partial f_j}{\partial x} \end{bmatrix}$$

$$G = \begin{bmatrix} \rho v \\ \rho uv + \tau_{yx} \\ \rho v^2 + \tau_{yy} \\ (\rho E + \tau_{yy}) v + \tau_{xy} u + q_{cy} + q_{ry} \\ \rho v f_j - \rho D \frac{\partial f_j}{\partial y} \end{bmatrix} \quad H = \begin{bmatrix} 0 \\ 0 \\ 0 \\ 0 \\ -\dot{W}_j \end{bmatrix}$$

The viscous stress tensors in the F and G terms of Eq. (2.1) are given as

$$\tau_{xx} = p - \lambda \left(\frac{\partial u}{\partial x} + \frac{\partial v}{\partial y} \right) - 2\mu \frac{\partial u}{\partial x} \quad (2.2a)$$

$$\tau_{xy} = -\mu \left(\frac{\partial u}{\partial y} + \frac{\partial v}{\partial x} \right) \quad (2.2b)$$

$$\tau_{yy} = p - \lambda \left(\frac{\partial u}{\partial x} + \frac{\partial v}{\partial y} \right) - 2\mu \frac{\partial v}{\partial y} \quad (2.2c)$$

The quantities q_{cx} and q_{cy} in the F and G terms are the components of the conduction heat flux and are expressed as

$$q_{cx} = -k \frac{\partial T}{\partial x} - \rho D \sum_{j=1}^m \left[\left(\frac{\partial f_j}{\partial x} \right) h_j \right] \quad (2.3a)$$

$$q_{cy} = -k \frac{\partial T}{\partial y} - \rho D \sum_{j=1}^m \left[\left(\frac{\partial f_j}{\partial y} \right) h_j \right] \quad (2.3b)$$

where

$$h_j = h_j^0 + \int_{T_0}^T C_p j dT; \quad T_0 = 0 \text{ K}$$

It should be noted here that D represents the effective binary diffusion coefficient and is used for all species. Assuming that the Lewis number is unity, Eqs. (3) reduce to (see Appendix A)

$$q_{cx} = - \frac{\gamma \mu}{Pr} \frac{\partial e}{\partial x} \quad (2.4a)$$

$$q_{cy} = - \frac{\gamma \mu}{Pr} \frac{\partial e}{\partial y} \quad (2.4b)$$

where

$$e = h - P/\rho$$

The molecular viscosity μ is assumed to be temperature dependent and it is evaluated for individual species from the Sutherland's formula

$$\mu = \mu_0 \left(\frac{T}{T_0} \right)^{3/2} \frac{T_0 + S}{T + S} \quad (2.5)$$

where μ_0 and T_0 are reference values and S is the Sutherland constant. The total internal energy E in Eq. (2.1) is given by

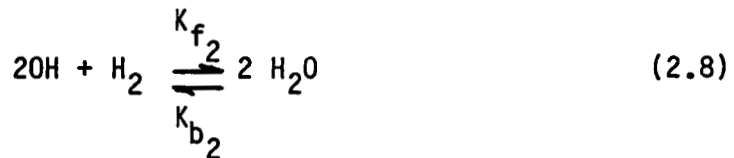
$$E = - P/\rho + \frac{u^2 + v^2}{2} + \sum_{i=1}^m h_i f_i \quad (2.6)$$

Specific relations are needed for the chemistry and thermodynamic models and for the radiative transport. The chemistry and thermodynamic models are discussed briefly in the following sections. The formulations for the radiative transport are presented in Sec. 3.

2.3 Chemistry Model

For the numerical solution of reacting flows, a chemistry model is needed to represent the combustion process. The chemistry model used in this study is the two-step global finite rate hydrogen-air combustion model developed by

Rogers and Chinitz [20]. This chemistry model was deduced from a 28 reaction model and it is adequate for temperatures between 1,000 K and 2,000 K and for equivalence ratios between 0.2 and 2.0. In the first step, hydrogen and air react and produce hydroxyl radical and in the second step, hydroxyl radical and hydrogen react to produce water vapor. The reactions are expressed as



where K_{f_i} and K_{b_i} represent the forward and reverse reaction rate constants respectively. The relations for K_{f_i} are obtained from an Arrhenius equation as

$$K_{f_i} = A_i(\phi) T^{N_i} \exp(-E_i/RT) \quad (2.9)$$

The values of the parameters $A_i(\phi)$, N_i , and E_i in Eq. (2.14) are

$$A_1(\phi) = (8.917 \phi + 31.433/\phi - 28.95) \times 10^{47} \sim \text{cm}^3/\text{g-mol-s}$$

$$E_1 = 4865 \text{ Cal/mol}; N_1 = -10.$$

$$A_2(\phi) = (2. + 1.333/\phi - .833\phi) \times 10^{64} \sim \text{cm}^6/\text{mol}^2 \cdot \text{s}$$

$$E_2 = 42500 \text{ Cal/mol}; N_2 = -13$$

where ϕ is the fuel-air ratio. The reverse rate constants can be evaluated by

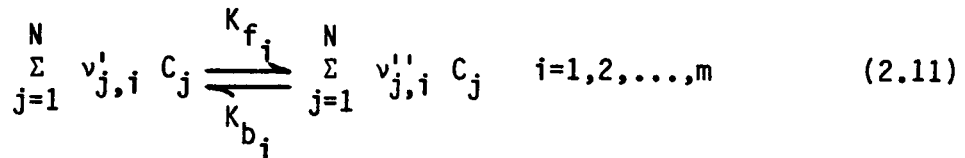
$$K_{b_i} = \frac{K_{f_i}}{K_i} \quad (2.10)$$

where

$$K_1 = 26.164 \exp(-8992/T)$$

$$K_2 = (2.682 \times 10^{-6}) (T) \exp(69415/T)$$

Knowing the reaction rates (K_{f_i} and K_{b_i}), the production of species can be evaluated from the law of mass action. Consider the general chemical reaction



where $v'_{j,i}$ and $v''_{j,i}$ represent the stoichiometric coefficients of the reactants and products respectively. The law of mass action states that the rate of change of concentration of species j by reaction i is given by [21]

$$(\dot{c}_j) = (v''_{ji} - v'_{ji}) [K_{f_i} \prod_{j=1}^N c_j^{v'_{ji}} - K_{b_i} \prod_{j=1}^N c_j^{v''_{ji}}] \quad (2.12)$$

The net rate of production of species j in all reactions is given by

$$\dot{c}_j = \sum_{i=1}^m (\dot{c}_j)_i \quad (2.13)$$

where m is the number of reactions. Finally, the chemistry source terms, on a mass basis, are found by multiplying the molar changes and corresponding molecular weight

$$\dot{w}_j = \dot{c}_j M_j \quad (2.14)$$

By applying the law of mass action to the global model, the chemistry source terms of the four species are obtained as

$$\dot{c}_{O_2} = -K_{f1} c_{H_2} c_{O_2} + K_{b1} c_{OH}^2 \quad (2.15)$$

$$\dot{c}_{H_2O} = 2(K_{f2} c_{OH}^2 c_{H_2} - K_{b2} c_{H_2O}^2) \quad (2.16)$$

$$\dot{c}_{H_2} = \dot{c}_{O_2} - 1/2 \dot{c}_{H_2O} \quad (2.17)$$

$$\dot{c}_{OH} = - (2 \dot{c}_{O_2} + \dot{c}_{H_2O}) \quad (2.18)$$

2.4 Thermodynamic Model

The specific heat of individual species, c_{p_i} , assumed to be a linear function of temperature, i.e.,

$$c_{p_j} = a_j T + b_j \quad (2.19)$$

where a_j and b_j are constants which are obtained by curve fitting the thermochemical data of Ref. 22. The numerical values of these constants are given in Table 1. The specific heat of the mixture are computed by summing specific heat of individual species weighted by species mass fraction

$$\bar{c}_p = \sum_{i=1}^m c_{p_j} f_j \quad (2.20)$$

The static enthalpy of the mixture can be expressed as

$$h = \sum_{j=1}^m [h_j^0 + \int_{T_0}^T c_{p_j} dT] f_j \quad (2.21)$$

The total enthalpy can now be evaluated as

$$H = h + 0.5 (u^2 + v^2) \quad (2.22)$$

Combining Eqs. (2.21) and (2.22), the total enthalpy is expressed as

$$H = \sum_{i=1}^m [h_i^0 + \frac{a_i T^2}{2} + b_i T] f_i + 0.5 (u^2 + v^2) \quad (2.23)$$

where h_i^0 is the sensible enthalpy of individual species at a reference temperature ($T_0 = 0$ K). The gas constant for the mixture also is evaluated by a mass weighted summation over all the species as

$$\bar{R} = \sum_{j=1}^m f_j R_j \quad (2.24)$$

The equation of state for the mixture of the gases, therefore can be written as

$$P = P\bar{R}T \quad (2.25)$$

Table 2.1 Numerical Values of Various Constants

Species	H°(J/kg)	a	b
O ₂	-271267.025	0.119845	947.937
H ₂ O	-13972530.24	0.43116	1857.904
H ₂	-4200188.095	2.0596	12867.46
OH	+1772591.157	0.16564	1672.813
N ₂	-309483.98	0.10354	1048.389

3. RADIATION TRANSPORT MODELS

In order to include the effects of radiative interaction in a physical problem, it is essential to accurately model the absorption-emission characteristics of participating species and provide a correct formulation of the radiative transfer processes. These are discussed briefly in this section.

3.1 Radiation Absorption Models

Many models are available in the literature to represent the absorption-emission characteristics of molecular species; a review of important models is available in [11]. Perhaps the simplest model is the gray gas model where the absorption coefficient is assumed to be independent of the wavelength. Many nongray models are also available in the literature. Both gray and nongray absorption models are discussed here briefly.

3.1.1 Gray Gas Models

In gray model, it is assumed that the absorption coefficient is independent of wavelength. This is rarely a physically realistic approximation but it serves as an initial step for studying the effect of radiative heat transfer. The absorption coefficient for gray gas is evaluated by employing the Planck mean absorption coefficient as follows

$$\kappa_p = \frac{\int_0^{\infty} \kappa_{\omega} e_{bw}(T) d\omega}{e_b(T)} \quad (3.1)$$

By assuming that within a band the Planck function does not vary significantly with the wave number and evaluating its value at the band center, the relation for κ_p for a single-band gas can be written as

$$\kappa_p = \frac{c_{b\omega_0}(T)}{\sigma T^4(y)} \int_{\Delta\omega} \kappa_\omega d\omega \quad (3.2)$$

where ω_0 represents the band center. For a multiband gaseous system, κ_p is given by

$$\kappa_p = \sum_{k=1}^n \left[\frac{e_{b\omega_k}(T)}{\sigma T^4(y)} \int_{\Delta\omega} \kappa_\omega d\omega \right] \quad (3.3)$$

where ω_k represents the band center of the k th band of a particular species. For a specific band of a given gas, the integrated band intensity S_k is defined as

$$S = \frac{1}{P_j} \int_{\Delta\omega} \kappa_\omega d\omega \quad (3.4)$$

Substituting Eq. (3.4) into Eq. (3.3), κ_p is expressed as

$$\kappa_p = \frac{P_j}{\sigma T^4(y)} \sum_{k=1}^n e_{b\omega_k}(T) S_k(T) \quad (3.5)$$

where

$$e_{b\omega_k}(T) = \frac{C_1 \omega_k^3}{\exp[C_2 \omega_k/T] - 1}$$

The P_j is species partial pressure and C_1 and C_2 are constants. Note that κ_p is a function of temperature and species partial pressure.

3.1.2 Nongray Gas Models

Important nongray models available in the literature are as follow:

1. Line Models:

- (a) Lorentz
- (b) Doppler

(c) Lorentz-Doppler (Voigt)

2. Narrow Band Models

- (a) Elsasser
- (b) Statistical
- (c) Random-Elsasser
- (d) Quasi-Random

3. Wide Band Models

- (a) Box or Coffin
- (b) Modified box
- (c) Exponential
- (d) Axial

The relative importance and range of applicability of these models are discussed in [11]. In the moderate temperature range (500-5000K) use of the wide band models and correlations provide sufficient accuracies. These models render significant computational efficiency over the line by line or narrow band models.

The expression for the total band absorptance is given as

$$A(y) = \int_0^{\infty} [1 - \exp(-\kappa_{\omega} y)] d\omega \sim \text{cm}^{-1} \quad (3.6a)$$

where both, ω and κ_{ω} have units of cm^{-1} . Differentiation of Eq. (3.6a) gives

$$A'(y) = \int_0^{\infty} \kappa_{\omega} \exp(-\kappa_{\omega} y) d\omega \sim \text{cm}^{-2} \quad (3.6b)$$

$$A''(y) = \int_0^{-\infty} -\kappa_{\omega}^2 \exp(-\kappa_{\omega} y) d\omega \sim \text{cm}^{-3} \quad (3.6c)$$

The radiative flux term usually involves multiple integrals even for the simple geometries. As result numerical calculation of radiative flux for energy transfer between two parallel plates becomes very time consuming. Therefore it is desirable to replace the relation for the total band absorptance as given by Eq. (3.6a) with a continuous correlation [6-9].

Numereous correlations are available in the literature for the wide band absorptance. The first correlation to satisfy the linear, square-root, and logarithmic limits of the wide band absorptance was proposed by Edward and Menard [23]. The most widely used correlation is the Tien and Lowder continuous correlation and this is given by [6]

$$\bar{A} = \ln [uf(\beta) (\frac{u+2}{u+2f(\beta)}) + 1.] \quad (3.7)$$

where

$$f(\beta) = 2.94 [1-\exp(-2.6\beta)]$$

$$\beta = B^2 P_e$$

The form of $f(\beta)$ was chosen to give agreement with the correlation of Edward and Menard. This correlation is employed in this study for nongray gas formulation.

3.2 Radiative Flux Equations

The equations of radiative transport are expressed generally in integro-differential form; the integration involves both frequency spectrum and physical coordinates. In many realistic three-dimensional physical problem, the complexity of the radiative transport equations can be overcome by introduction of the "trangent slab approximation." This approximation treats the gas layers as a one-dimensional slab in evaluation of the radiative flux. Tangent slab approximation is employed in this study. Therefore, the radiative transport is considered only in the normal direction of the flow. It should be pointed out that this approximation is not used for any other flow variables.

3.2.1 Basic Formulation

The radiative transport equations in the present study are obtained for a gas confined between two parallel plates (Fig. 5.1). For one-dimensional absorbing-emitting medium with diffuse boundaries the general equation for the radiative flux under the condition of thermodynamic equilibrium (LTE) is given by [5, 8, 24].

$$q_{R\lambda} = 2 B_{1\lambda} E_3 (\tau_\lambda) - 2 B_{2\lambda} E_3 (\tau_{0\lambda} - \tau_\lambda)$$

$$+ 2\pi \int_0^{\tau_\lambda} B_\lambda(t) E_2 (\tau_\lambda - t) dt - 2\pi \int_{\tau_\lambda}^{\tau_{0\lambda}} B_\lambda(t) E_2 (t - \tau_\lambda) dt \quad (3.8)$$

where

$$\tau_\lambda = \kappa_\lambda y; \quad \tau_{0\lambda} = \kappa_\lambda L$$

The quantities $B_{1\lambda}$ and $B_{2\lambda}$ in Eq. (3.8) represent the spectral surface radiosities, and for non-reflecting surfaces $B_{1\lambda} = e_{1\lambda} = \epsilon_{1\lambda} e_{b1\lambda}$. For non-reflecting surfaces under the conditions of LTE the expression for the spectral radiative flux is expressed in terms of the wave number as (see Appendix B)

$$q_{R\omega}(\tau_\omega) = e_{1\omega} - e_{2\omega} + 2 \{ \int_0^{\tau_\omega} [e_\omega(t) - e_{1\omega}] E_2 (\tau_\omega - t) dt \\ - \int_{\tau_\omega}^{\tau_{0\omega}} [e_\omega(t) - e_{2\omega}] E_2 (t - \tau_\omega) dt \} \quad (3.9)$$

where $E_n(t)$ is an exponential integral function defined by

$$E_n(t) = \int_0^1 \mu^{n-2} e^{-t/\mu} d\mu; \quad \int E_n(t) dt = - E_{n+1}(t)$$

By employing the exponential kernel approximation [5]

$$E_2(t) = \frac{3}{4} e^{-\frac{3}{4}t} ; E_1(t) = \frac{9}{8} e^{-\frac{3}{2}t} \quad (3.10)$$

Eq. (3.9) is expressed as

$$\begin{aligned} q_{R\omega}(\tau_\omega) &= e_{1\omega} - e_{2\omega} + \frac{3}{2} \left\{ \int_0^{\tau_\omega} F_{1\omega}(t) e^{-\frac{3}{2}(\tau_\omega-t)} dt \right. \\ &\quad \left. - \int_{\tau_\omega}^{\tau_{0\omega}} F_{2\omega}(t) e^{-\frac{3}{2}(t-\tau_\omega)} dt \right\} \end{aligned} \quad (3.11)$$

where

$$F_{1\omega}(t) = e_\omega(t) - e_{1\omega} ; F_{2\omega}(t) = e_\omega(t) - e_{2\omega}$$

Equation (3.11) is expressed in physical coordinate as

$$\begin{aligned} q_{R\omega}(y) &= e_{1\omega} - e_{2\omega} + \frac{3}{2} \int_0^y F_{1\omega}(z) \kappa_\omega \exp[-\frac{3}{2} \kappa_\omega(y-z)] dz \\ &\quad - \frac{3}{2} \int_y^L F_{2\omega}(z) \kappa_\omega \exp[-\frac{3}{2} \kappa_\omega(z-y)] dz \end{aligned} \quad (3.12)$$

By differentiating Eq. (3.12) with respect to y , one obtains

$$\begin{aligned} \frac{-d q_{R\omega}(y)}{dy} &= \frac{9}{4} \int_0^y F_{1\omega}(z) \kappa_\omega^2 \exp[-\frac{3}{2} \kappa_\omega(y-z)] dz \\ &\quad + \frac{9}{4} \int_y^L F_{2\omega}(z) \kappa_\omega^2 \exp[-\frac{3}{2} \kappa_\omega(z-y)] dz \\ &\quad - \frac{3}{2} \kappa_\omega [F_{1\omega}(y) + F_{2\omega}(y)] \end{aligned} \quad (3.13)$$

The total radiative flux is given by

$$q_R(y) = \int_0^\infty q_{R\omega}(y) d\omega \quad (3.14a)$$

such that

$$\frac{dq_R(y)}{dy} = \int_0^\infty \frac{dq_{R\omega}}{dy} d\omega = \frac{d}{dy} \int_0^\infty q_{R\omega} d\omega \quad (3.14b)$$

It should be noted here that for nongray gases, the divergence of radiative flux is used as a source term in the energy equation to avoid a scheme dependency in the computation.

3.2.2 Gray Formulation

In the previous section, it was observed that the radiative flux terms are represented by an integro-differential equation. Solving these equations are very time consuming, even with the vector processor such as VPS-32. Therefore, a pesudo-gray model is selected for efficient parametric studies. To express the radiative flux for a gray medium, one may assume that κ_ω is now independent of the wave number. Therefore, Eq. (3.9) for a gray medium is written as

$$q_R(\tau) = e_1 - e_2 + 2 \int_0^\tau [e(t) - e_1] E_2(\tau - t) dt \\ - 2 \int_\tau^0 [e(t) - e_2] E_2(t - \tau) dt \quad (3.15)$$

Upon substituting the exponential kernal approximation, Eq. (3.10), into Eq. (3.15), $q_R(\tau)$ is expressed as

$$q_R(\tau) = e_1 - e_2 + \frac{3}{2} \left\{ \int_0^\tau [e(t) - e_1] e^{-\frac{3}{2}(\tau-t)} dt \right. \\ \left. - \int_\tau^0 [e(t) - e_2] e^{-\frac{3}{2}(t-\tau)} dt \right\} \quad (3.16)$$

To solve the radiative flux term for the gray medium, one can transform Eq. (3.15) into the physical coordinates and then apply any of the standard integration techniques to evaluate the radiative flux term. If this is desirable, then there is no need to make exponential kernal approximation and obtain Eq. (3.16). The main reason for employing the exponential kernal approximation in the gray formulation is to transform the integral equation into a differential equation. Solving a radiative flux equation in differential form is not only convenient but computationally efficient. For the present case, differentiating Eq. (3.16) twice by using the Leibnitz rule results in

$$\frac{d^2 q_R(\tau)}{d\tau^2} = \frac{9}{4} \left\{ \frac{3}{2} \int_0^\tau [e(t) - e_1] e^{-\frac{3}{2}(t-\tau)} dt - \frac{3}{2} \int_\tau^{t_0} [e(t) - e_2] e^{-\frac{3}{2}(t-\tau)} dt \right\} + (e_1 - e_2) + 3 \frac{de(\tau)}{d\tau} \quad (3.17)$$

A substitution of Eq. (3.17) into Eq. (3.16) gives a second order nonhomogenous ordinary differential equation as

$$\frac{d^2 q_R(\tau)}{d\tau^2} - \frac{9}{4} q_R(\tau) = 3 \frac{de(\tau)}{d\tau} \quad (3.18)$$

It should be pointed out that if Eq. (3.15) is differentiated and then Kernal approximation is applied the coefficient on the right side of Eq. (3.18) will be four. Employing the method of differential approximation instead of exponential kernal approximation, Eq. (3.15) may be recast as a differential equation which is of the same form as Eq. (3.18), except the coefficient of the second differential is 3/4 instead of unity [5]. Equation (3.18) requires two boundary conditions, which for nonblack diffuse surfaces are given as (see Appendix C).

$$\left(\frac{1}{\epsilon_1} - \frac{1}{2}\right) q_R(\tau) \Big|_{\tau=0} - \frac{1}{3} \frac{dq_R}{d\tau} \Big|_{\tau=0} = e_{b_1} - e_b(0) \quad (3.19a)$$

$$\left(\frac{1}{\epsilon_2} - \frac{1}{2}\right) q_R(\tau) \Big|_{\tau=\tau_0} + \frac{1}{3} \frac{dq_R}{d\tau} \Big|_{\tau=\tau_0} = e_b(\tau_0) - e_{b_2} \quad (3.19b)$$

Note that the right sides of Eqs. (3.19) differ from zero only if molecular conduction is neglected. In this study, other modes of energy transfer are included. Therefore, the terms on right sides reduce to zero.

To evaluate the radiative flux, Eqs. (3.18) and (3.19) are transformed into the physical coordinates as

$$\frac{d^2 q_R(y)}{d(\kappa_p y)^2} - \frac{9}{4} q_R(y) = 3 \frac{de(y)}{d(\kappa_p y)} \quad (3.20a)$$

$$\left(\frac{1}{\epsilon_1} - \frac{1}{2}\right) q_R(y) \Big|_{y=0} - \frac{1}{3} \frac{dq_R}{d(\kappa_p y)} \Big|_{y=0} = 0 \quad (3.20b)$$

$$\left(\frac{1}{\epsilon_2} - \frac{1}{2}\right) q_R(y) \Big|_{y=L} + \frac{1}{3} \frac{dq_R}{d(\kappa_p y)} \Big|_{y=L} = 0 \quad (3.20c)$$

The optical coordinate and thickness used in the above transformation are defined as

$$\tau = \kappa_p y ; \tau_0 = \kappa_p L$$

3.2.3 Nongray Formulation

The radiative flux equation for nongray gases is obtained by substituting Eq. (3.13) into Eq. (3.14) as

$$\begin{aligned} \frac{-dq_R}{dy} &= \frac{9}{4} \int_0^\infty \left\{ \int_0^y F_{1\omega}(z) \kappa_\omega^2 \exp[-\frac{3}{2} \kappa_\omega(y-z)] dz \right. \\ &\quad \left. + \int_y^L F_{2\omega}(z) \kappa_\omega^2 \exp[-\frac{3}{2} \kappa_\omega(z-y)] dz \right\} d\omega \end{aligned}$$

$$-\frac{3}{2} \int_0^\infty \kappa_\omega [F_{1\omega}(y) + F_{2\omega}(y)] d\omega \quad (3.21)$$

For a multi-band gaseous system, the above is expressed as

$$\begin{aligned} \frac{-dq_R}{dy} = & \frac{9}{4} \sum_{i=1}^n \int_{\Delta\omega_i} \left\{ \int_0^y F_{1\omega_i}(z) \kappa_{\omega_i}^2 \exp[-\frac{3}{2} \kappa_{\omega_i} (y-z)] dz \right. \\ & \left. + \int_y^L F_{2\omega_i}(z) \kappa_{\omega_i}^2 \exp[-\frac{3}{2} \kappa_{\omega_i} (z-y)] dz \right\} d\omega_i \\ = & -\frac{3}{2} \sum_{i=1}^N \int_{\Delta\omega_i} [F_{1\omega_i}(y) + F_{2\omega_i}(y)] d\omega_i \end{aligned} \quad (3.22)$$

It should be pointed out that the following relation has been employed to obtain Eq. (3.22)

$$\begin{aligned} & \int_0^\infty \left\{ \int_0^y F_{1\omega}(z) \kappa_\omega \exp[-\frac{3}{2} \kappa_\omega (y-z)] dz \right\} d\omega \\ = & \sum_{i=1}^N \int_{\Delta\omega_i} \left\{ \int_0^y F_{1\omega_i}(z) \kappa_{\omega_i} \exp[-\frac{3}{2} \kappa_{\omega_i} (y-z)] dz \right\} d\omega_i \end{aligned}$$

where N represent the number of bands in a multiband system. Now, utilizing the definition of band absorptance and its derivatives as given in Eqs. (3.6), and evaluating the value of Planck function at the center of each band Eq. (3.22) is expressed as

$$\begin{aligned} \frac{dq_R(y)}{dy} = & \frac{3}{2} \sum_{i=1}^N \{ [F_{1\omega_{oi}}(y) + F_{2\omega_{oi}}(y)] \left(\int_{\Delta\omega_i} \kappa_{\omega_i} d\omega_i \right) \} \\ & + \frac{9}{4} \sum_{i=1}^N \left\{ \int_0^y F_{1\omega_{oi}}(z) A_i^{'''} \left[\frac{3}{2} (y-z) \right] dz \right. \\ & \left. + \int_y^L F_{2\omega_{oi}}(z) A_i^{'''} \left[\frac{3}{2} (z-y) \right] dz \right\} \end{aligned} \quad (3.23)$$

Equation (3.23) is in proper form for obtaining the nongray solutions of molecular species. However, in order to be able to use the band model correlations, these equations must be transformed in terms of the correlation quantities. The correlation quantities and detail of transformations are given in Ref. 24. After the transformation, Eq. (3.23) is written as

$$\begin{aligned} \frac{dq_R(u)}{du} = & \frac{9}{4} \sum_{i=1}^N A_{0i} \left\{ \int_0^{u_i} F_{1\omega_i}(u') \bar{A}_i'' \left[\frac{3}{2} (u_i - u'_i) \right] du'_i \right. \\ & + \left. \int_{u'_i}^{u_{0i}} F_{2\omega_i}(u') \bar{A}_i'' \left[\frac{3}{2} (u'_i - u_i) \right] du'_i \right\} \\ & + \frac{3}{2} \sum_{i=1}^N A_{0i} [F_{1\omega_i}(u) + F_{2\omega_i}(u)] \end{aligned} \quad (3.24)$$

Note that $\bar{A}''(u)$ express the second derivative of $\bar{A}(u)$ with respect to u and

$$\frac{dq_R}{dy} = \frac{dq_R}{du} \frac{du}{dy} = [\text{PS}(T)/A_0] \frac{dq_R}{du}$$

By defining $\frac{u}{u_0} = \frac{y}{L}$ and $\frac{u'}{u_0} = \frac{z}{L}$ Eq. (3.29) is expressed as

$$\begin{aligned} \frac{dq_R(y)}{dy} = & \frac{9}{4} \sum_{i=1}^N \frac{A_0 u_0^2}{L^2} \left\{ \int_0^y F_{1\omega_i}(z) \bar{A}_i'' \left[\frac{3}{2} \frac{u_0}{L} (y - z) \right] dz \right. \\ & + \left. \int_y^L F_{2\omega_i}(u') \bar{A}_i'' \left[\frac{3}{2} (u'_i - u_i) \right] du'_i \right\} \\ & + \frac{3}{2} \sum_{i=1}^N \frac{A_0 u_0}{L} [F_{1\omega_i}(z) + F_{2\omega_i}(z)] \end{aligned} \quad (3.25)$$

It is often desirable and convenient to express the above equation in terms of \bar{A}' rather than \bar{A}'' . This is accomplished by integrating Eq.

(3.25) by parts. The details of the integration by parts is given in Ref. 24 and the result is given by

$$\frac{dq_R}{dy} = \frac{3}{2} \sum_{i=1}^N \frac{A_{o_i} u_{o_i}}{L} \left\{ \int_0^y \frac{de_{\omega_i}(z)}{dz} \bar{A}' \left[\frac{3}{2} \frac{u_{o_i}}{L} (y - z) \right] dz \right. \\ \left. - \int_y^L \frac{de_{\omega_i}(z)}{dz} \bar{A}' \left[\frac{3}{2} \frac{u_{o_i}}{L} (z - y) \right] dz \right\} \quad (3.26)$$

Equation (3.26) and the Tien and Lowder correlation given by Eq. (3.7) can be used to evaluate the radiative flux.

4. METHOD OF SOLUTION

The grid generation and solution procedures for the governing equations are briefly discussed in this section.

4.1 Grid Generation

The grids are generated using an algebraic grid generation technique similar to the one used by Smith and Weigel [25]. From the computational point of view, it is desirable to have uniform rectangular grid enclosed in parallel piped, and the exterior of the parallel piped represent the physical boundaries. To have such grids, the body-fitted coordinate is transformed linearly from physical domain (x,y) to computational domain (ξ,η) as follow

$$\begin{aligned} x_1 &= \underline{x}(\xi, 0) \\ y_1 &= \underline{y}(\xi, 0) \end{aligned} \quad \left. \begin{array}{l} \text{Lower} \\ \text{Boundary} \end{array} \right\} \quad (4.1a)$$

$$\begin{aligned} x_2 &= \underline{x}(\xi, 1) \\ y_2 &= \underline{y}(\xi, 1) \end{aligned} \quad \left. \begin{array}{l} \text{Upper} \\ \text{Boundary} \end{array} \right\} \quad (4.1b)$$

$$\left. \begin{array}{l} x = \underline{x}(\xi, 1) \eta + \underline{x}(\xi, 0) (1-\eta) \\ y = Y(\xi, 1) \eta + y(\xi, 0) (1-\eta) \end{array} \right\} \text{Between the Boundaries} \quad (4.1e)$$

where

$$0 < \xi < 1 ; 0 < \eta < 1$$

The grid should be concentrated in the regions of high gradient to accurately capture the solution. Therefore more grids are required near the solid boundaries. The concentration of the grid in η direction can be accomplished by

$$\bar{\eta} = \frac{(\beta_y + 1) - (\beta_y - 1) \exp[-C(\eta-1+\alpha)/(1-\alpha)]}{(2\alpha+1) \{1+\exp[1C(\eta-1+\alpha)/(1-\alpha)]\}} \quad (4.2)$$

where

$$C = \ln \left(\frac{\beta_y + 1}{\beta_y - 1} \right)$$

If α is equal to zero ($\alpha=0$) the compression takes place only near the lower wall ($\eta=0$), and if, α is set equal to one half ($\alpha=1/2$), the compression takes place near both walls. The β_y has a value between one and two, and as it gets closer to one, the grid becomes more concentrated near the walls. Employing this concentration, Eq. (4.1e) in terms of $\bar{\eta}$ is written as

$$\begin{aligned} x &= \underline{x}(\xi, 1) \bar{\eta} + \underline{x}(\xi, 0) (1-\bar{\eta}) \\ y &= Y(\xi, 1) \bar{\eta} + y(\xi, 0) (1-\bar{\eta}) \end{aligned} \quad (4.3)$$

where

$$0 < \bar{\eta} < 1$$

The grid used in this study is shown in Fig. 4.1. It should be noticed that the grid is concentrated in the normal direction and kept uniform in the flow direction.

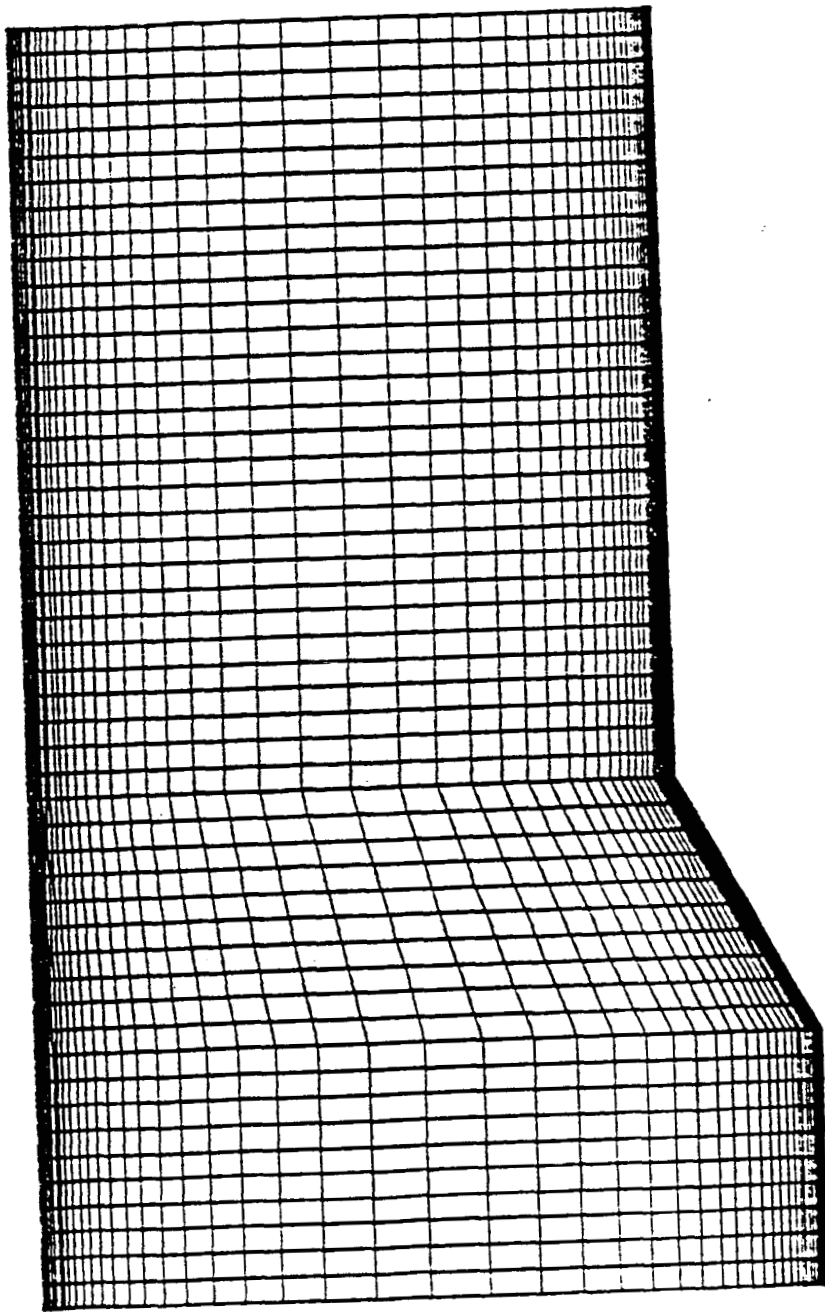


Fig. 4.1 Grid structure.

4.2 Solution of the Governing Equations

The governing equations, Eqs. (2.1), are expressed in the computational domain as

$$\frac{\partial \hat{U}}{\partial t} + \frac{\partial \hat{F}}{\partial \xi} + \frac{\partial \hat{G}}{\partial \eta} + \hat{H} = 0 \quad (4.4)$$

where

$$\hat{U} = UJ$$

$$\hat{F} = Fy_\eta - Gx_\eta$$

$$\hat{G} = Gx_\xi - Fy_\xi$$

$$\hat{H} = HJ$$

$$J = x_\xi y_\eta - y_\xi x_\eta$$

Equation (4.4) is discretized temporally and written as

$$\hat{U}^{n+1} = \hat{U}^n - \Delta t \left[\frac{\partial \hat{F}}{\partial \xi} + \frac{\partial \hat{G}}{\partial \eta} + \hat{H}^{n+1} \right] \quad (4.5)$$

$$\hat{H}^{n+1} = \hat{H}^n + \Delta t \frac{\partial \hat{H}}{\partial t} \quad (4.6)$$

$$\hat{H}^{n+1} = \hat{H}^n + \Delta t \frac{\partial H}{\partial U} \left(\frac{\hat{U}^{n+1} - \hat{U}^n}{\Delta t} \right) \quad (4.7)$$

A substitution of Eq. (4.7) into Eq. (4.5) gives the temporally discrete equation in delta form as

$$\left[I + \Delta t \frac{\partial H}{\partial U} \right] \Delta \hat{U}^{n+1} = -\Delta t \left[\frac{\partial \hat{F}}{\partial \xi} + \frac{\partial \hat{G}}{\partial \eta} + \hat{H}^n \right] \quad (4.8)$$

where $\hat{U}^{n+1} - \hat{U}^n$ is expressed as $\Delta \hat{U}^{n+1}$, $\frac{\partial H}{\partial U}$ is the Jacobian matrix of H and I is the identity matrix.

Once the temporal discretization used to construct Eq. (4.8) has been

performed, the resulting system is spatially differenced using the unsplit MacCormack predictor-corrector scheme [26]. This results in a spatially and temporally discrete, simultaneous system of equations at each grid point [16-17]. Each simultaneous system is solved using the Householder technique [27, 28] in combination with the MacCormack technique which is then used to advance the equations in time. The modified MacCormack scheme then becomes

$$[I + \Delta t \left(\frac{\partial \hat{H}}{\partial U} \right)_{ij}^n] \Delta \hat{U}_{ij}^{n+1} = - \Delta t \left[\frac{\partial \hat{F}}{\partial \xi} + \frac{\partial \hat{G}}{\partial \eta} + \hat{H} \right]_{ij}^n \quad (4.9a)$$

$$\hat{U}_{ij}^{n+1} = \hat{U}_{ij}^n + \Delta \hat{U}_{ij}^{n+1} \quad (4.9b)$$

$$[I + \Delta t \left(\frac{\partial \hat{H}}{\partial U} \right)_{ij}^n] \Delta \hat{U}_{ij}^{n+1} = - \Delta t \left[\frac{\partial \hat{F}}{\partial \xi} + \frac{\partial \hat{G}}{\partial \eta} + \hat{H} \right]_{ij}^{n+1} \quad (4.10a)$$

$$\hat{U}_{ij}^{n+1} = \hat{U}_{ij}^n + 0.5 [\Delta \hat{U}_{ij}^{n+1} + \Delta \hat{U}_{ij}^{n+1}] \quad (4.10b)$$

Equations (4.9) and (4.10) are used to advance the solution from time n to $n+1$ and this process is continued until a desired integration time has been reached.

For time accurate solution, the computational time step, Δt , must satisfy the smallest time scales of the fluid and chemistry, i.e., $\Delta t = \min(\Delta t_f, \Delta t_{ch})$. If the steady state solution is sought (as in this study), it is possible to speed up the convergence by using a larger time scale ($\Delta t_f = \Delta t_{CFL}$) without introducing any instabilities in the solution. This is due to the so-called precondition matrix (left-hand side bracket in Eq. (4.8)), the purpose of which is to normalize the various time scales so that they are of the same order [17].

The radiative flux term is evaluated for both gray and nongray gaseous systems. In the nongray gas formulation, the divergence of the radiative flux is evaluated using a central differencing scheme and is treated as radiative source term in the energy equation. Since the radiative flux term is in integro-differential form, unlike the other flux terms which are only in a differential form, it is uncoupled and treated separately. In the gray gas formulation, Eqs. (3.20) are discretized by central differencing, forming a tridiagonal matrix. This tridiagonal matrix can be solved efficiently by the Thomas algorithm.

5. RESULTS AND DISCUSSION

Based on the theory and computational procedure described in the previous sections, a computer code was developed to solve the two-dimensional Navier-Stokes equations for reacting and radiating supersonic laminar flows. Two different geometries are employed for various parametric studies. One is a channel with two parallel plates a distance L apart (Fig. 5.1); the other is a channel with a compression-expansion ramp at the lower boundary (Fig. 5.2). The freestream conditions at the inlet are obtained from Refs. 1-4. For the temperature range expected in the scramjet combustor, the radiating species that are important are OH and H₂O. The spectral information and correlation quantities needed for these species are obtained from Refs. 6-9 and 29. Both reacting and nonreacting flows are considered. Results for the nonreacting flows are presented in Figs. 5.3-5.10 and for the reacting flows results are presented in Figs. 5.11-5.16.

For the parallel plate case (3 cm x 10 cm), the inflow conditions are $P_{\infty} = 1$ atm, $T_{\infty} = 1,700$ K, $M_{\infty} = 3.0$, and $F_{H_2O} = 0.5$, $f_{O_2} = 0.1$ and $f_{N_2} = 0.4$. Results for the radiative flux, as a function of the nondimen-

sional location along the flow, are illustrated in Fig. 5.3 for various distances from the lower plate. It is noted that the radiation flux is approximately zero in the center of the plate ($y = 1.5$ cm) and is considerably higher towards the top and bottom plates. This, however, would be expected because of the symmetry of the problem and relatively higher temperature near the boundaries. The oscillations in results are due to the shock reflection from the boundaries.

The results for radiative flux are illustrated in Figs. 5.4 and 5.5 as a function of the nondimensional y -coordinate. For $P = 1$ atm, the results presented in Fig. 5.4 for different water vapor concentrations indicate that the radiative interaction increases slowly with an increase in the amount of the gas. The results for 50% H_2O are illustrated in Fig. 5.5 for two different pressures ($P_\infty = 1$ and 3 atm) and x -locations ($x=5$ and 10 cm). It is noted that the increase in pressure has dramatic effects on the radiative interaction. The conduction and radiation heat transfer results are compared in Fig. 6 for $P = 3$ atm and for two different x -locations ($x = 5$ and 10 cm). The results demonstrate that the conduction heat transfer is restricted to the region near the boundaries and does not change significantly from one x -location to another. The radiative interaction, however, is seen to be important everywhere in the channel, and this can have significant influence on the entire flowfield. The results presented in Figs. 5.4-5.6 should be physically symmetric; but, due to the predictor-corrector procedure used in the McCormack's scheme, they exhibit some unsymmetrical behavior.

For the parallel plate geometry, a comparison of the divergence of radiative flux for gray and nongray models is presented in Fig. 5.7 for two different y -locations ($y = 0.2$ and 1.6 cm). The physical and inflow conditions in this case are exactly the same as for Fig. 5.3. The gray gas

formulation is based on the Planck mean absorption coefficient which accounts for the detailed information on different molecular bands. As such, this approach is referred to as the "pseudo gray gas formulation." As mentioned before, Tien and Lowder's correlation (Ref. 6) is used in the nongray formulation. It is noted that the results for the gray model are about 10-20 percent higher than for the nongray model. For the physical conditions of the problem, no significant difference in results is observed for the two y -locations. Both gray and nongray results are seen to increase with x because the pressure and temperature, in general, increase in the flow direction. The solution of the gray formulation in ODE form proves to be about ten times more efficient than the solution of the nongray formulation on the VPS-32 computer (the gray formulation uses 0.056 CRU's per iteration while the nongray formulation uses 0.57 CRU's per iteration). As such, all other results presented in this study have been obtained by using the pseudo gray gas formulation.

The second geometry (Fig. 5.2) was selected to study the effects of shocks on the radiative heat transfer. The physical dimensions considered for obtaining specific results are $L = 3$ cm, $X_1 = 3$ cm, $X_2 = 3$ cm, $L_x = 10$ cm, and $\alpha = 10^0$. In general, the inlet conditions considered are the same as for the parallel plate geometry, i.e., $P_\infty = 1$ atm, $T_\infty = 1,700$ K, $f_{H_2O} = 0.5$. Results for this case at steady state are given in Figs. 5.8 and 5.9. For $M_\infty = 4.5$, only the resulting pressure contours are shown in Fig. 5.8 and the results for the radiative heat flux are illustrated in Fig. 5.9 for $M_\infty = 3$ and 4.5. The pressure contours clearly show the existence of the shock and expansion fan. The results presented in Fig. 5.9 show a significant increase in the radiative heat flux over the ramp for $M_\infty = 4.5$. The oscillatory behavior observed towards the end of the channel for $M_\infty = 3$ is

due to the effect of the shock reflection from the upper boundary. At both Mach numbers, only a slight variation in results is noted for different y-locations in the channel.

For the physical conditions of Fig. 5.2 and $M_\infty = 4.5$, the radiative flux results along the channel are compared in Fig. 5.10 at two different y-locations ($y = 0.0$ and 1.5 cm) and for two different compositions of gaseous mixture, $25\% \text{ H}_2\text{O} + 75\% \text{ air}$ and $25\% \text{ H}_2\text{O} + 25\% \text{ OH} + 50\% \text{ air}$. The results show that the radiative interaction is relatively higher for the case of $25\% \text{ H}_2\text{O}$ than for $25\% \text{ H}_2\text{O} + 25\% \text{ OH}$. It is quite likely that for the temperature and pressure range over the ramp, OH is highly effective in absorbing the radiative energy. The results for two different y-locations are seen to be essentially the same. It is possible that for the physical conditions of the problem, the radiative transfer process is closer to the optically thin limit; and, in this limit, the radiative flux is independent of the y-location (Refs. 29 and 30).

To investigate the effects of radiative energy transfer in chemically reacting flows, premixed hydrogen and air with an equivalence ratio of unity was selected. Specific results were obtained again for the geometry of Fig. 5.2 with the inlet conditions being exactly the same as for Fig. 5.8. For the physical conditions of the problem, the radiation participating species produced due to chemical reaction essentially are OH and H_2O . The radiative interaction is started at about $X/L_x = 0.20$ to make sure there are significant amounts of OH and H_2O produced by the reaction for active participation. The pressure contours for this case are shown in Fig. 5.11. A comparison of the pressure contours for the nonreacting and reacting flows as given in Figs. 5.8 and 5.11 shows that the shock angle has increased in the case of the reacting flow. This is due to a relatively thicker boundary layer and changes in the thermophysical properties of the mixture.

The distribution of various species at the lower boundary and center of the channel are illustrated respectively in Figs 5.12 and 5.13. Due to the high temperature, OH increases very rapidly over a short distance from the inlet and then remains constant for both y-locations. The concentration of OH is found to be higher near the boundaries due to relatively higher temperature. The rate of radiative flux along the channel is compared for this case in Fig. 5.14 for the reacting and nonreacting flows. For the nonreacting flow, the radiative flux is evaluated for 25% H₂O; while for the reacting flow, it is evaluated for H₂O and OH produced by the actual reaction. It is noted that although the amount of participating species is less in the reacting case, the radiative flux is considerably higher in this case than the nonreacting flow. This is due to the increase in temperature caused by the chemical reaction.

The variations in temperature and species concentration along the channel are illustrated respectively in Figs. 5.15 and 5.16 for chemically reacting, and chemically reacting and radiating flows. The results are obtained for exactly the same conditions as used in Figs. 5.11-5.14. The temperature variations in Fig. 5.15 are given for different y-locations. It is noted that the temperature within the boundary layer ($y = 0.025$) is about five percent higher for the reacting and radiating interaction. For other locations ($y = 0.2$ and 1.5 cm), no significant difference in the results for the two cases was noted. The variation in mass fraction for different species is shown in Fig. 5.16 within the boundary layer ($y = 0.025$ cm). It is found that due to the radiative interaction, the concentration of OH increases by about five percent and the concentration of H₂O decreases by the same amount. It should be noted that the radiative interaction has no significant effect on O₂ and H₂.

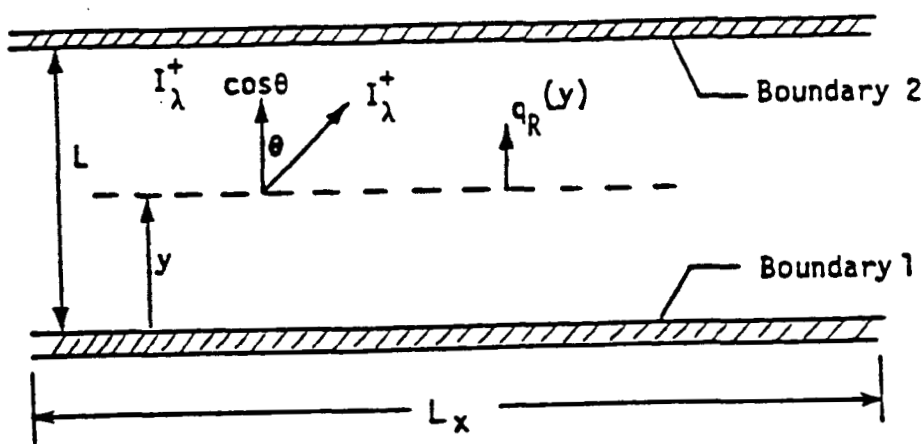


Fig. 5.1 Plane radiating layer between parallel boundaries.

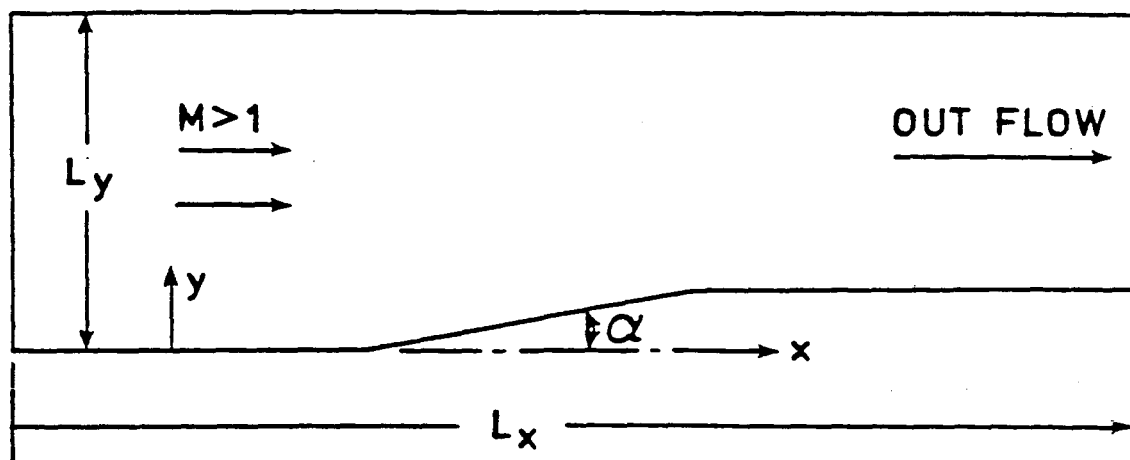


Fig. 5.2 Radiating flow in a channel with compression expansion ramp.

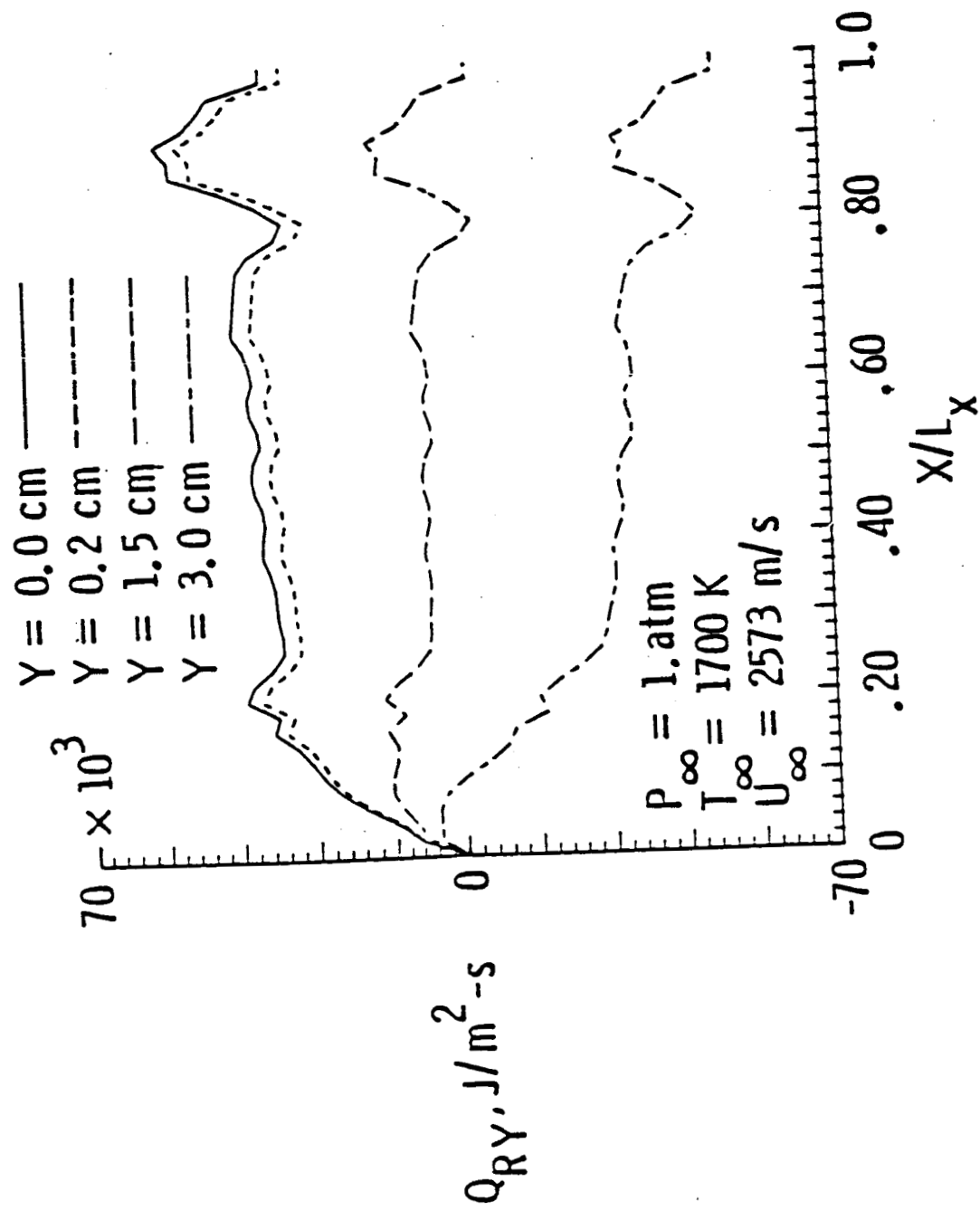


Fig. 5.3 Radiative flux along the channel for 50% H_2O .

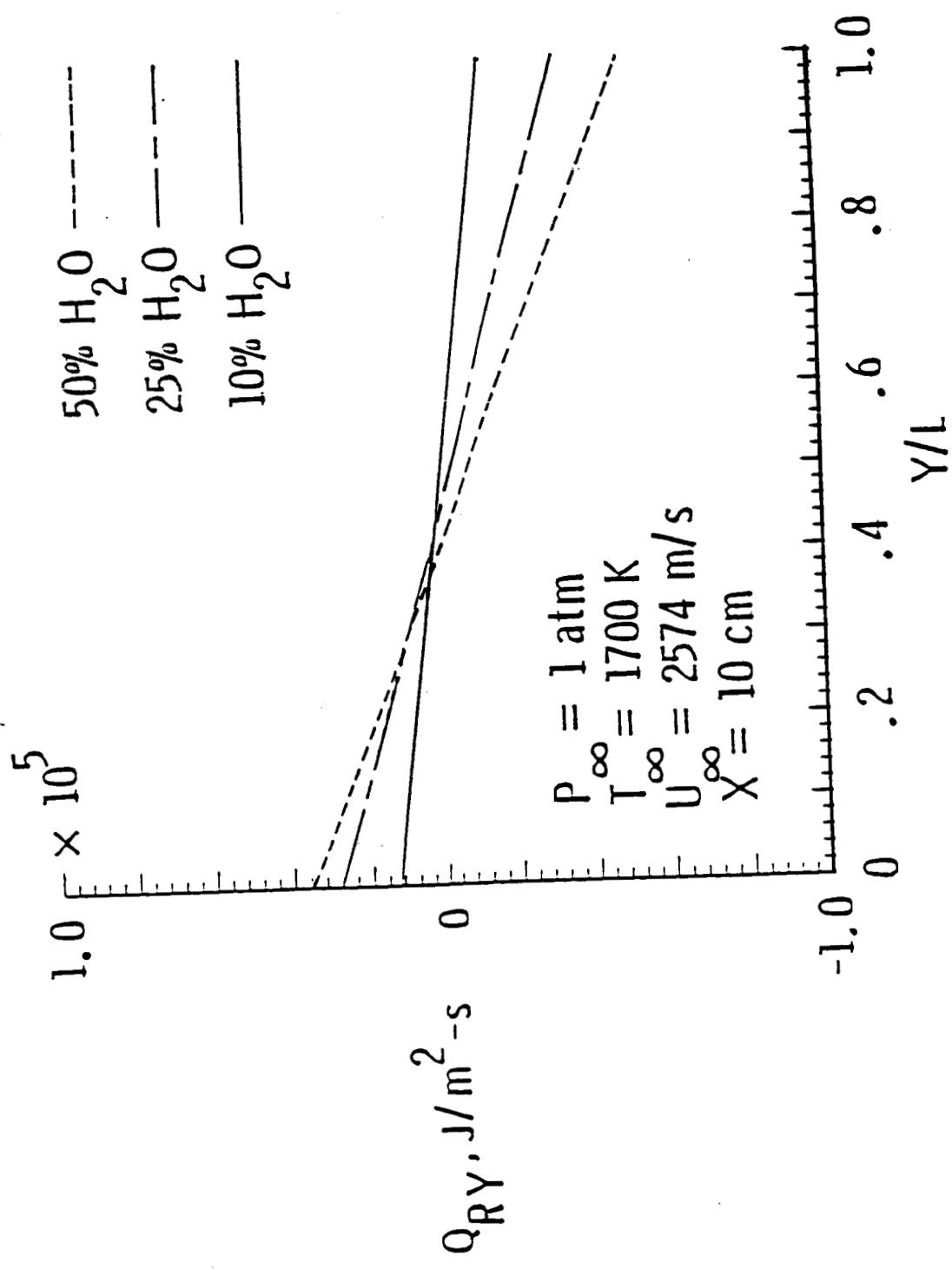


Fig. 5.4 Radiative flux vs. y at the channel exit.

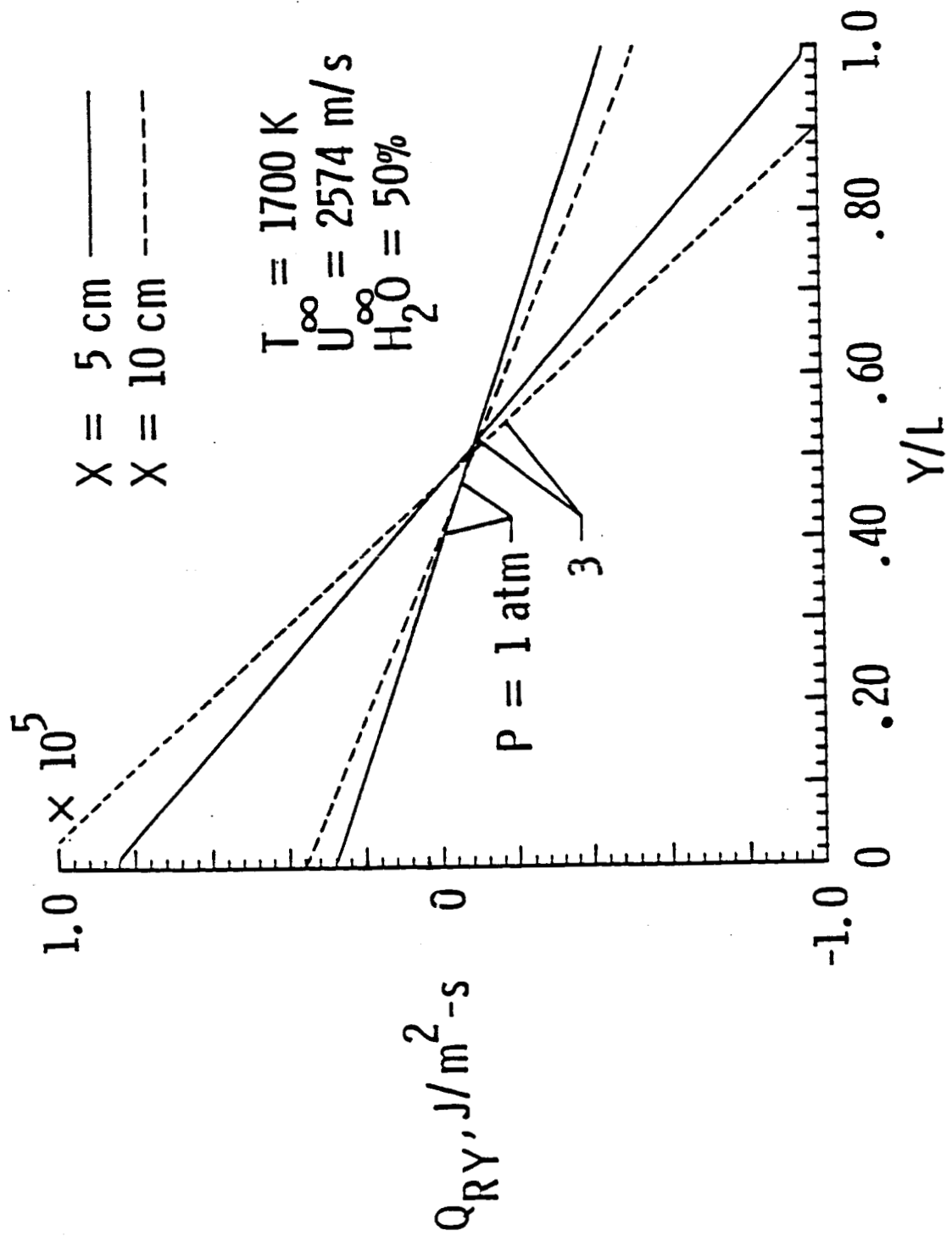


Fig. 5.5 Radiative flux vs. y at $x=5$ and 10 cm .

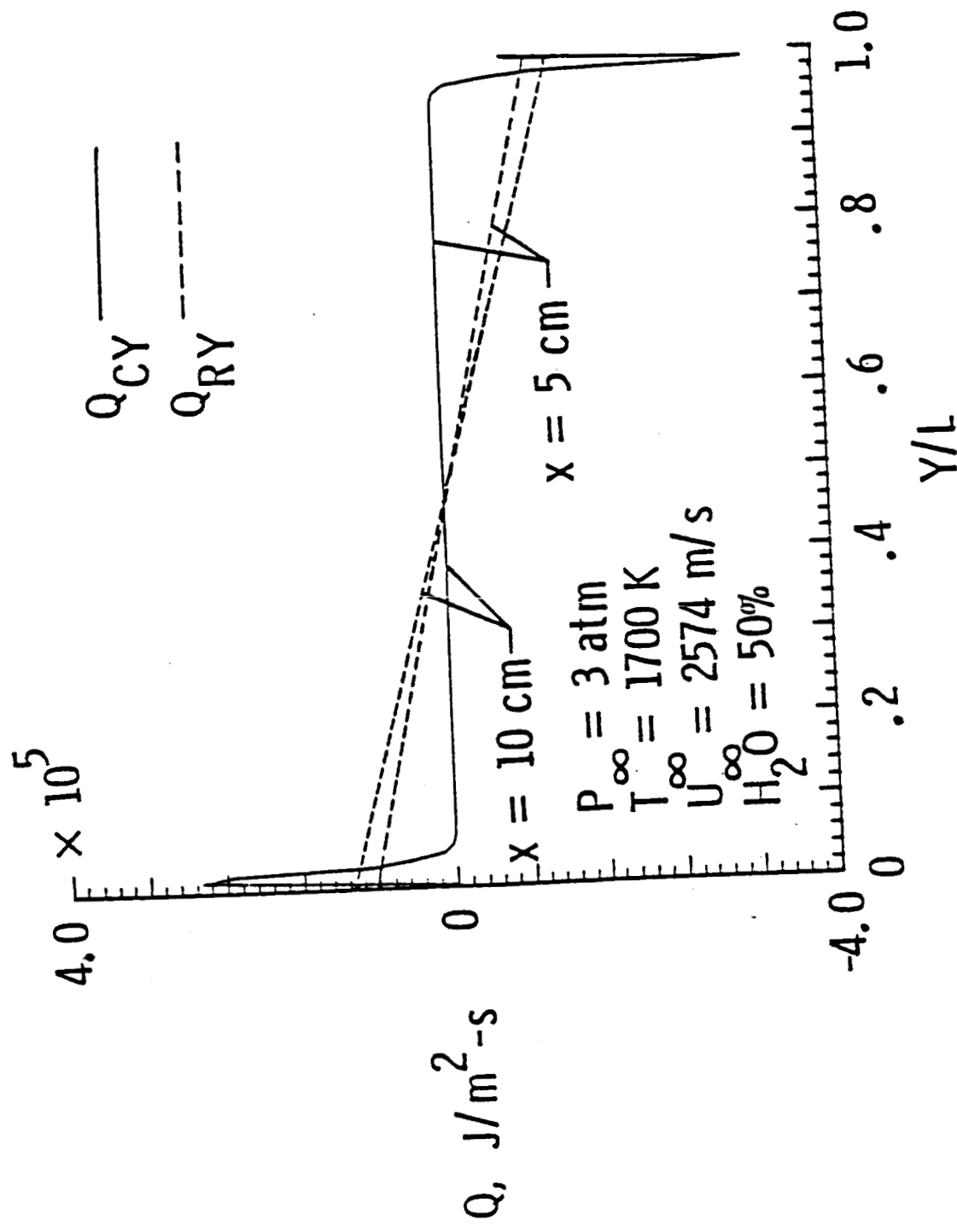


Fig. 5.6 Radiative and conductive flux vs. y at $x=5$ and 10 cm .

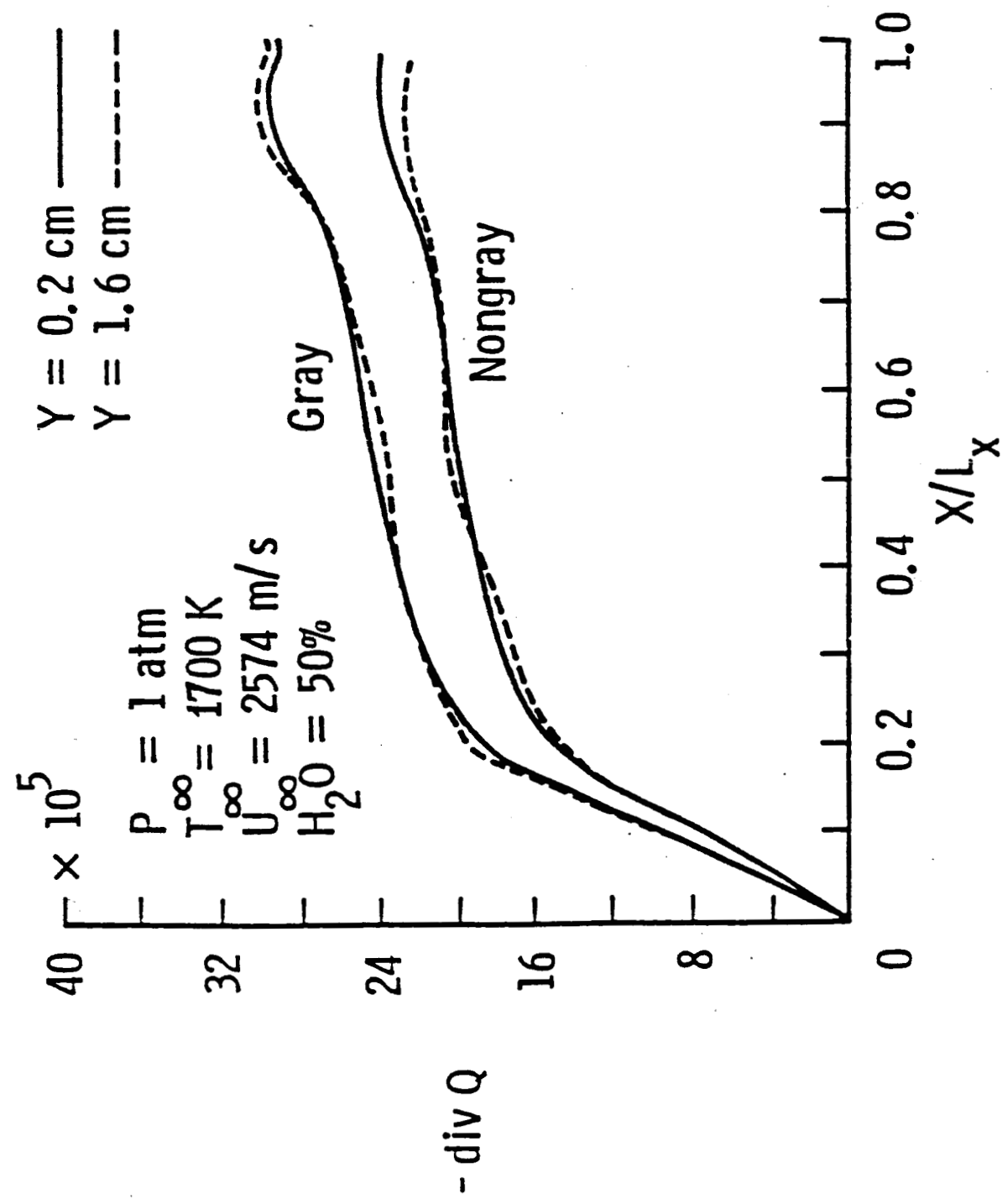


Fig. 5.7 Comparison of results for gray and nongray radiation.

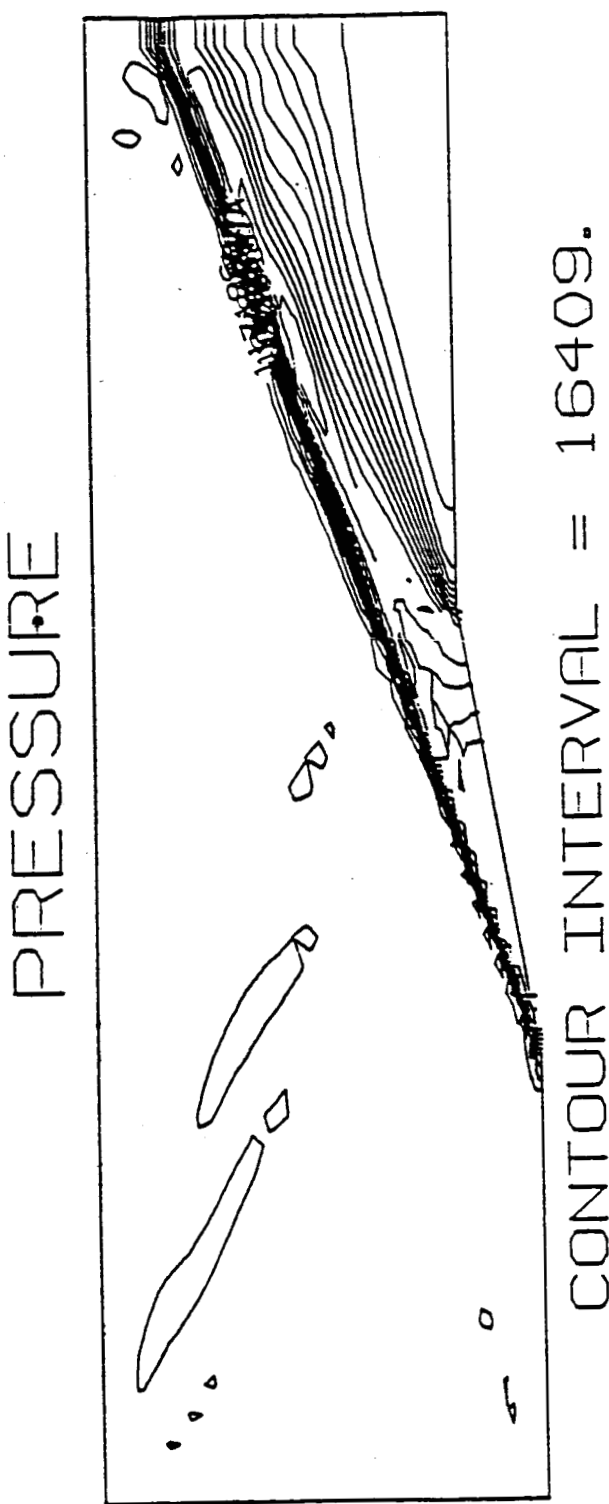


Fig. 5.8 Pressure contours for nonreacting flow in a channel with a ramp.

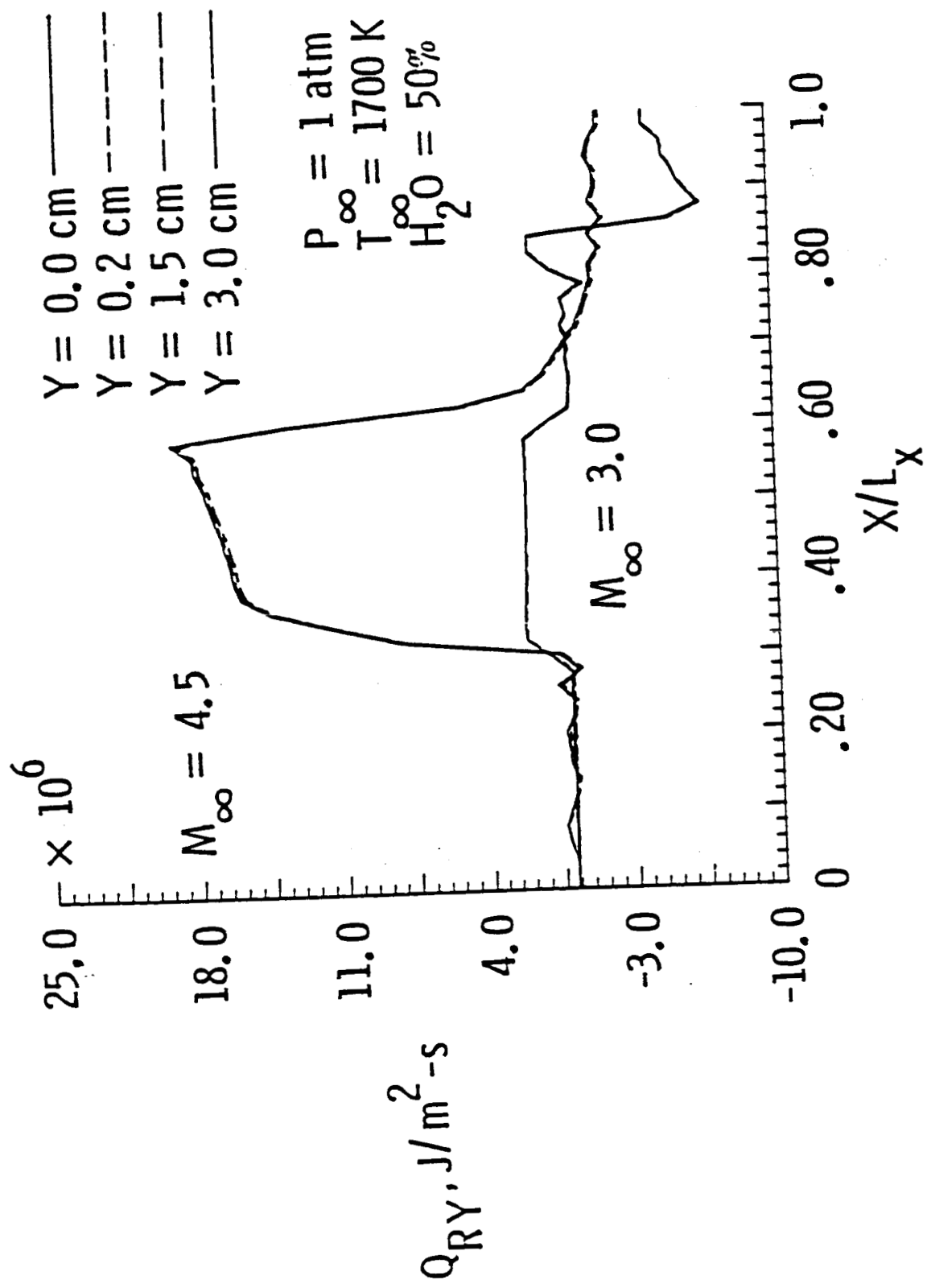


Fig. 5.9 Radiative flux vs. x for two different free-stream velocities.

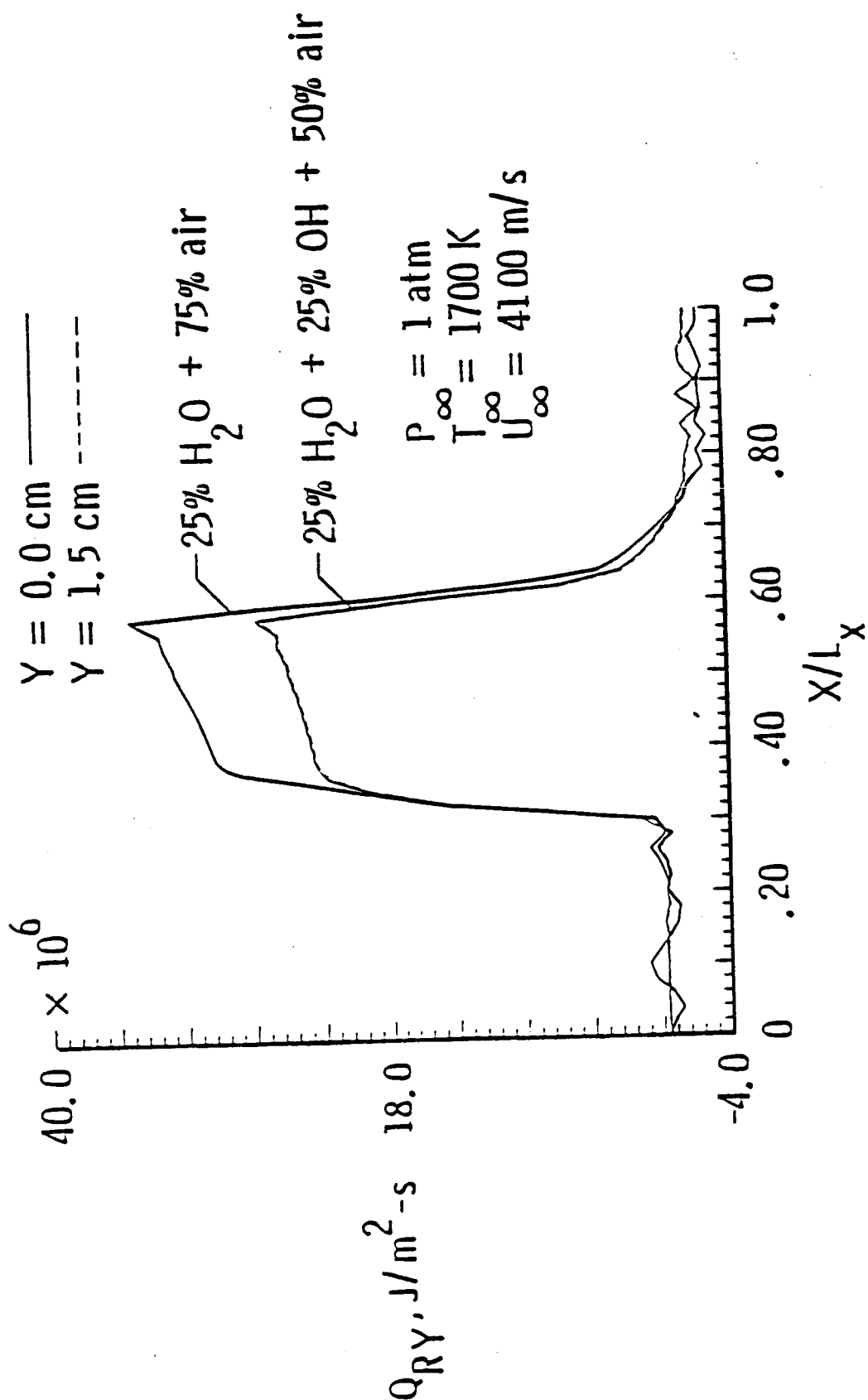


Fig. 5.10 Radiative flux vs. x for two different gas compositions.

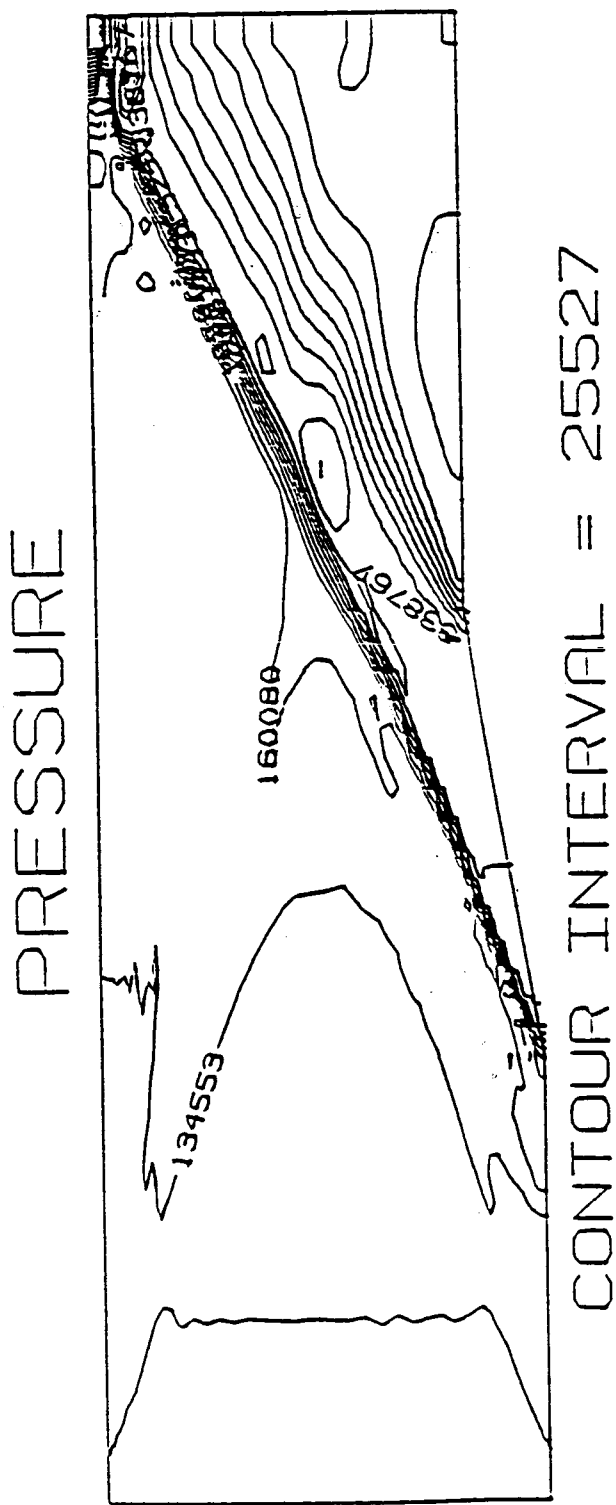


Fig 5.11 Pressure contours for reacting flow in a channel with a ramp.

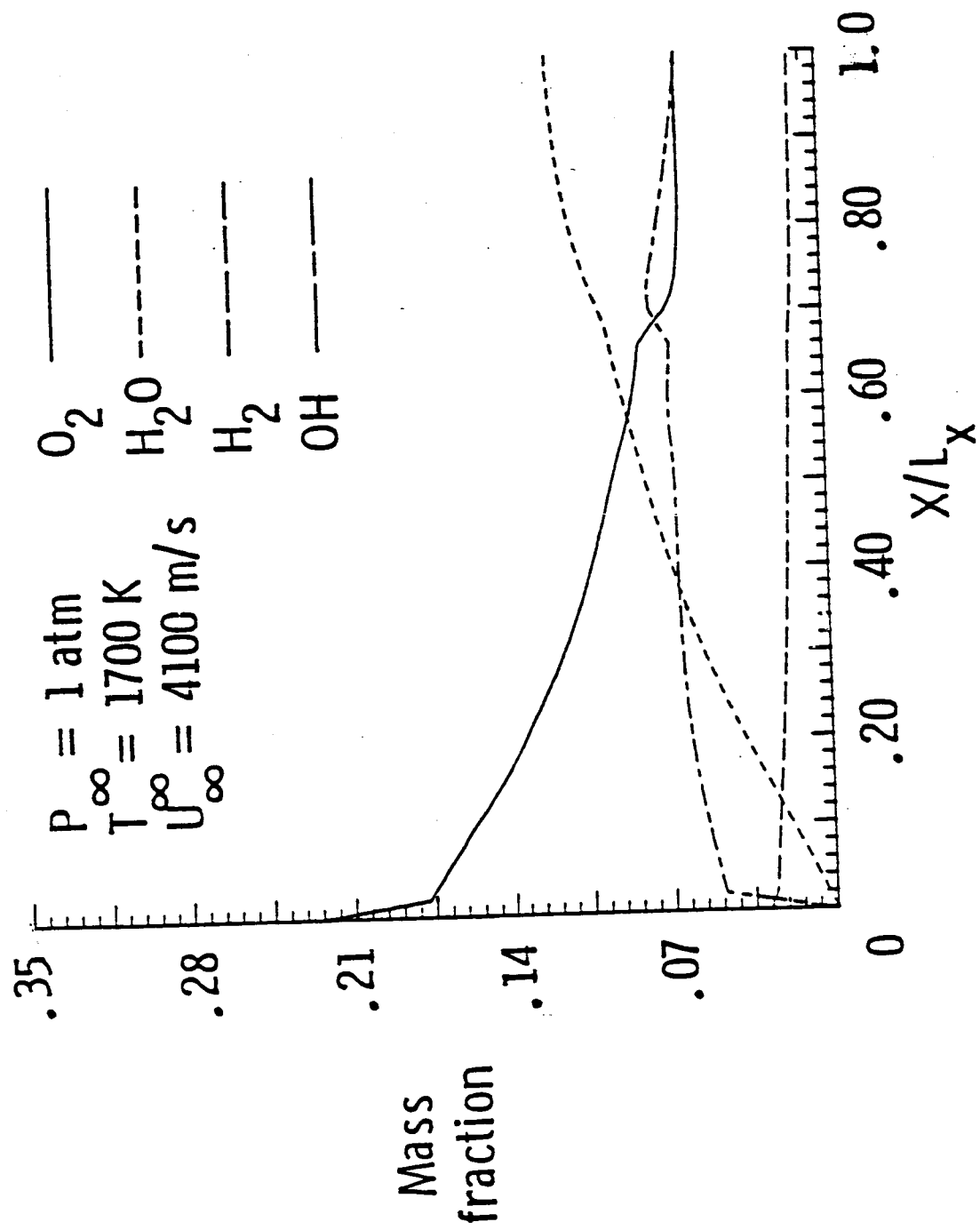


Fig. 5.12 Mass fraction vs. x at the lower boundary.

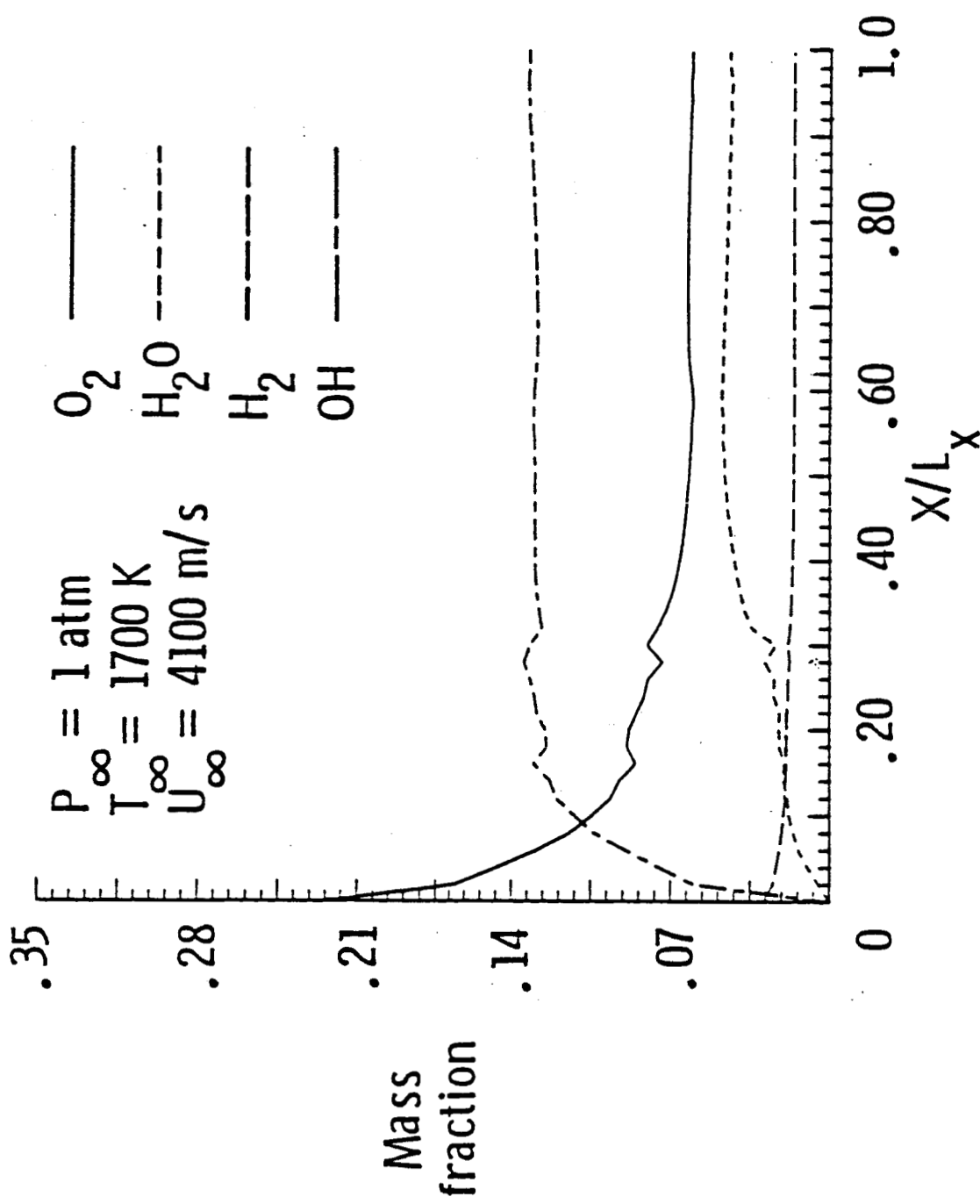


Fig. 5.13 Mass fraction vs. x at $y=1.5 \text{ cm}$.

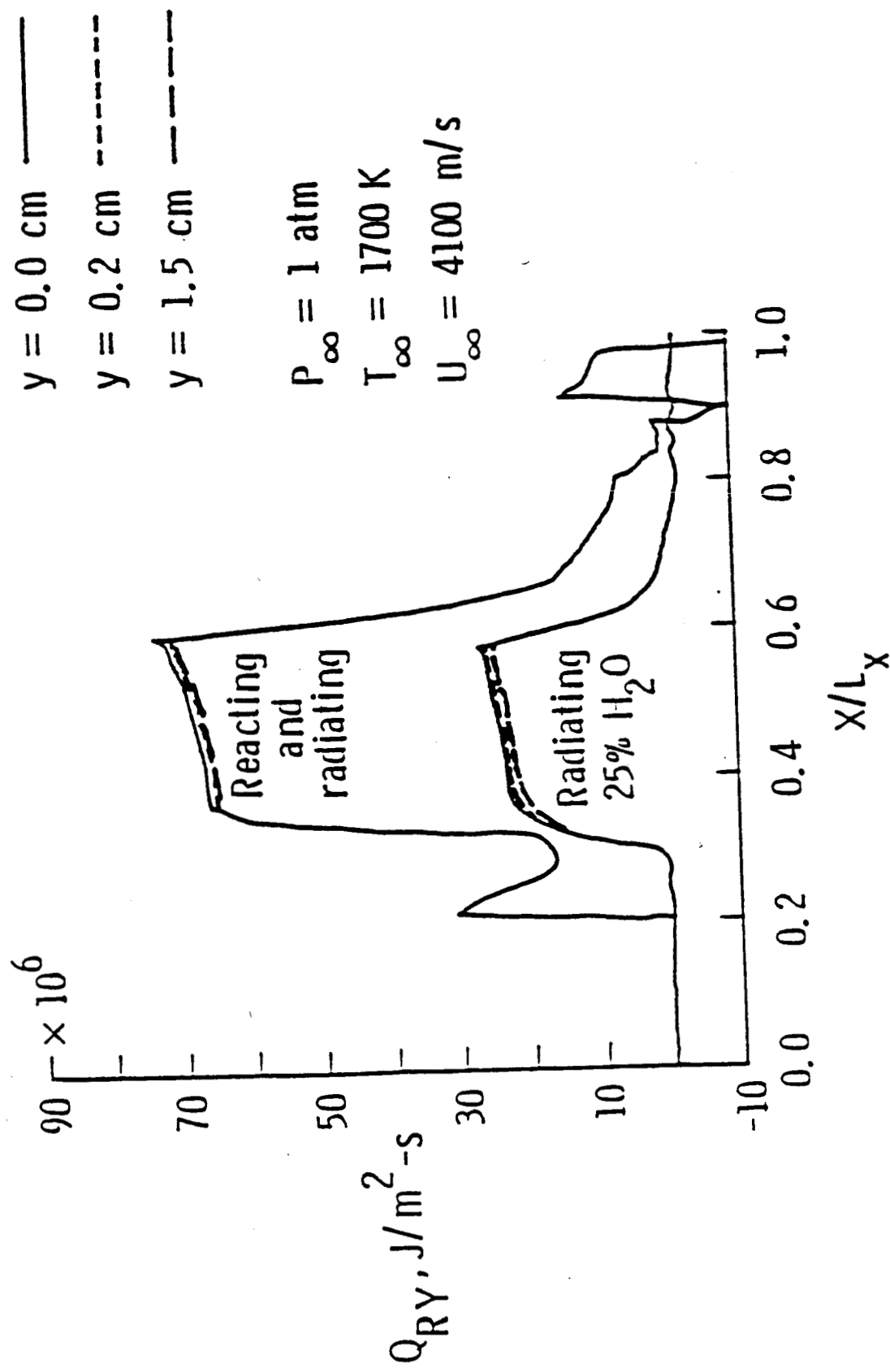


Fig. 5.14 Radiative flux vs. x for reacting and nonreacting flows.

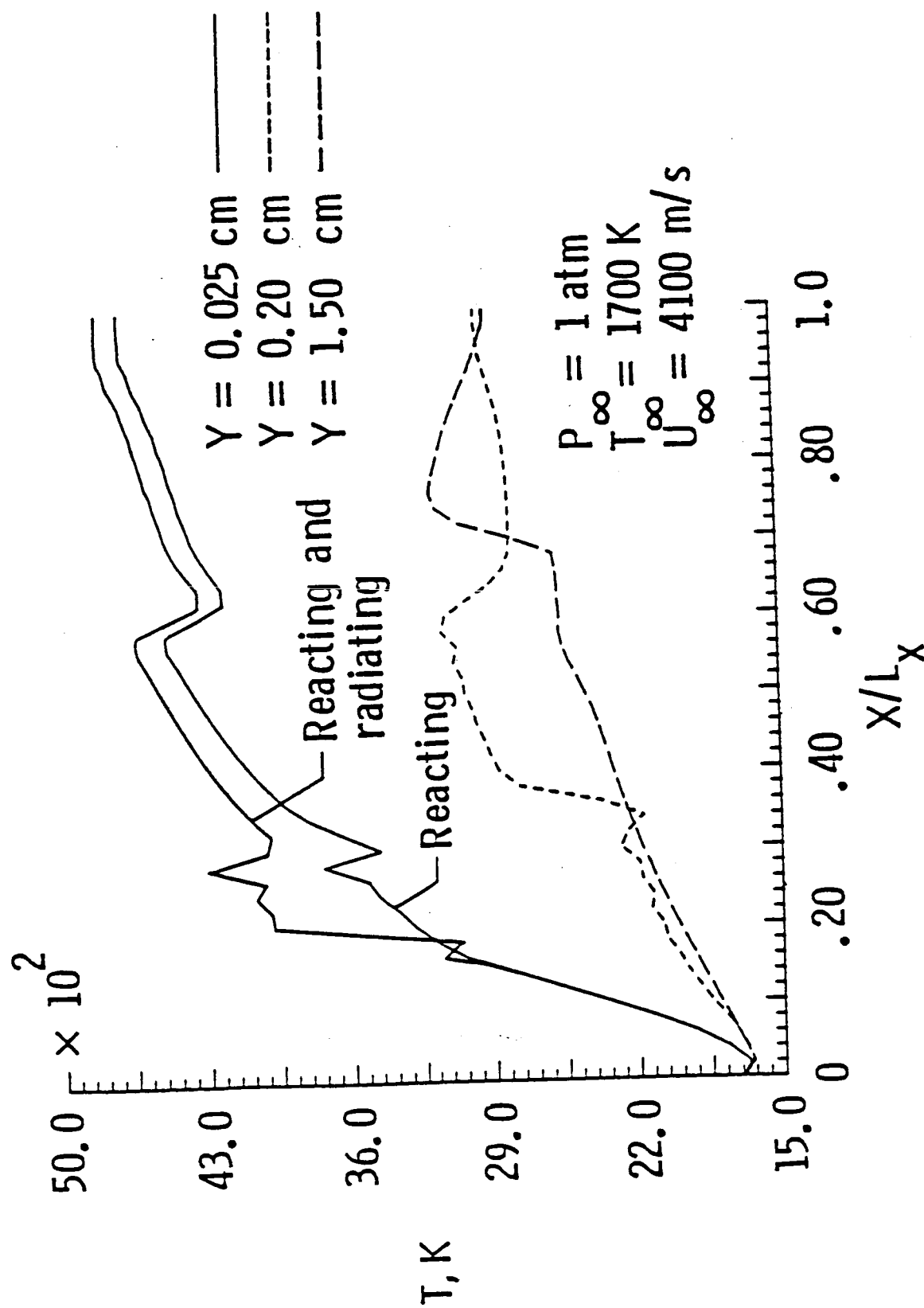


Fig. 5.15 Temperature vs. x for reacting and radiating flows.

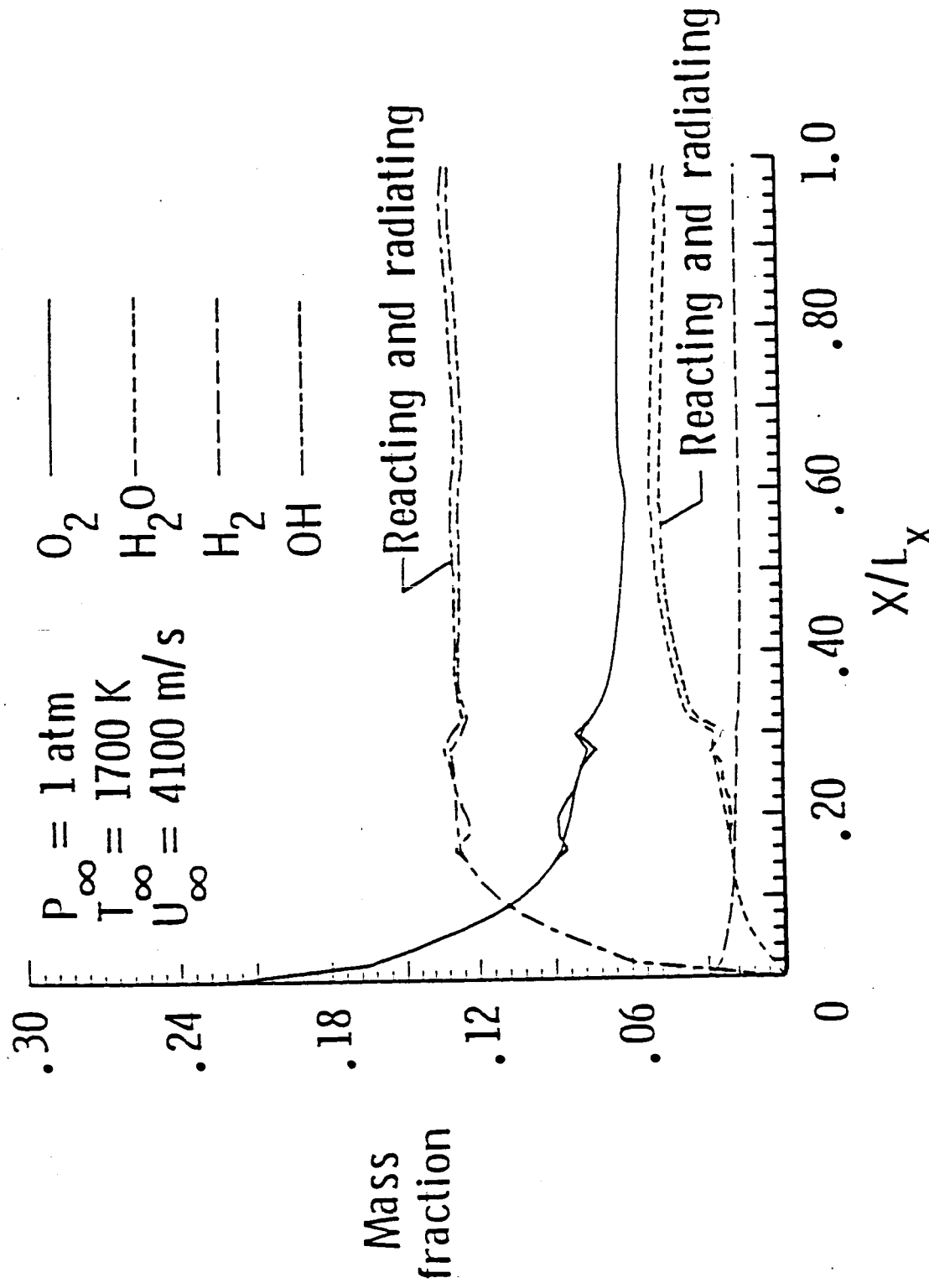


Fig. 5.16 Mass fraction vs. x for reacting and radiating flows.

6. CONCLUSIONS

The two-dimensional spatially elliptic Navier-Stokes equations have been used to obtain solutions for chemically reacting and radiating supersonic flow between two parallel plates and in a channel with a ten-degree ramp at the lower boundary. The inlet conditions used for specific solutions correspond to particular flow conditions of a scramjet engine. For both physical geometries, diagnostic solutions were obtained to investigate the influence of the radiative interaction without considering any chemical reaction. Different amounts of H₂O and OH were used with air for parametric studies. It is noted that the radiative interaction increases with increasing pressure, temperature, species concentration, and Mach number. In the case of flow without chemical reaction, most of the energy transferred is by convection in the direction of the flow. As a result, the radiative interaction does not affect the flow field significantly. Some important results were obtained by considering the reacting flow in the channel with a ramp. The results reveal that, in the case of flow with strong shocks, radiation can have significant influence on the entire flow field; however, the influence is stronger in the boundary layers. It is found that the numerical scheme based on the pseudo gray gas formulation for the radiative flux is highly efficient as compared to the scheme based on the nongray gas formulation, especially for the vector processing computers such as VPS-32. For further study, it is suggested that the present formulation be extended to include two-dimensional radiative interactions and provide parametric investigations for higher inlet Mach numbers.

REFERENCES

1. Kumar, A., "Numerical Analysis of a Scramjet Inlet Flowfield Using the Three-Dimensional Navier-Stokes Equations," presented at the 1983 JANAF Propulsion Meeting, February 1983; also "Numerical Simulation of Scramjet Inlet Flow Field," NASA TP-2517, May 1986.
2. Drummond, J. P., Hussaini, M. Y. and Zang, T. A., "Spectral Methods for Modeling Supersonic Chemically Reacting Flow Fields," AIAA Journal, Vol. 24, No. 9, 1986, pp. 1461-1467.
3. Drummond, J. P., Rogers, R. C. and Hussaini, M. Y., "A Detailed Numerical Model of a Supersonic Reacting Mixing Layer," AIAA Paper No. 86-1427, June 1986.
4. Chitsomboon, T., Kumar, A., Drummond, J. P. and Tiwari, S. N., "Numerical Study of Supersonic Combustion Using a Finite-Rate Chemistry Model," AIAA Paper No. 86-0309, January 1986; also, Chitsomboon, T. and Tiwari, S. N., "Numerical Study of Hydrogen-Air Supersonic Combustion By Using Elliptic and Parabolized Equations," Progress Report NAG-1-423, Dept. of Mechanical Engineering and Mechanics, Old Dominion University, Norfolk, VA, August 1986.
5. Sparrow, E. M. and Cess, R. D., Radiation Heat Transfer, Brooks/Cole, Belmont, CA, 1966 and 1970; New Augmented Edition, Hemisphere Publishing Corp., Washington, D.C., 1978.
6. Tien, C. L. and Lowder, J. G., "A Correlation for Total Band Absorptance of Radiating Gases," International Journal of Heat and Mass Transfer, Vol. 9, July 1966, pp. 698-701.
7. Tien, C. L., "Thermal Radiation Properties of Gases," Advances in Heat Transfer, Vol. 5, Academic Press, New York, 1968.
8. Cess, R. D. and Tiwari, S. N., "Infrared Radiative Energy Transfer in Gases," Advances in Heat Transfer, Vol. 8, Academic Press, New York, 1972.
9. Edwards, D. K., "Molecular Gas Band Radiation," Advances in Heat Transfer, Vol. 12, Academic Press, New York, 1976.
10. Tiwari, S. N., "Band Models and Correlations for Infrared Radiation," Radiative Transfer and Thermal Control (Progress in Astronautics and Aeronautics), Vol. 49, American Institute of Aeronautics and Astronautics, New York, 1976.
11. Tiwari, S. N., "Models for Infrared Atmospheric Radiation," Advances in Geophysics, Vol. 20, Academic Press, New York, 1978, pp. 1-85.
12. James R. K. and Edwards, D. K., "Effect of Molecular Gases Radiation on a Planar, Two-Dimensional, Turbulent-Jet-Diffusion Flame," Journal of Heat Transfer, Vol. 99, May 1977.

13. Tiwari, S. N., "Application of Infrared Band Model Correlations to Nongray Radiation," International Journal of Heat and Mass Transfer, Vol. 20, July 1977, pp. 741-751.
14. Vincent, L., Lloyd, J. R. and Yang, K. T., "An Investigation of a Laminar Diffusion Flame Adjacent to a Vertical Flat Plate Burner," International Journal of Heat and Mass Transfer, Vol. 24, No. 12, December 1981, pp. 1959-1970.
15. Smoot, L. D., Hecker, W. C. and Williams, G. A., "Prediction of Propagating Methane-Air Flames," Combustion and Flame, Vol. 26, 1976.
16. Stalnaker, J. F., Robinson, M. A., Spradley, L. W., Kurzius, S. C. and Theoeres D., "Development of the General Interpolants Methods for the Cyber 200 Series of Computers," Report TR 0867354, Lockheed-Huntsville Research and Engineering Center, Huntsville, AL, October 1983.
17. Bussing, T. R. A. and Murman, E. M., "A Finite Volume Method for the Calculation of Compressible Chemically Reacting Flows," AIAA Paper No. 85-0331, January 1985.
18. Jones, R. A., Huber, P. W., "Toward Scramjet Aircraft," NASA CP-2065-Pt. 1, 1978, pp. 30-48.
19. Beach, H. L., "Hypersonic Propulsion," NASA CP-2092, 1979, pp. 387-407.
20. Rogers, R. C. and Chinitz, W., "Using a Global Hydrogen-Air Combustion Model in Turbulent Reacting Flow Calculation," AIAA Journal, Vol. 21, No. 4, April 1983.
21. Williams, F. A., Combustion Theory, Second Edition, Benjamin/Cummings Publishing Company, Inc., Menlo park, California, 1985.
22. McBride, B. J., Heimel, S., Ehlens, J. G. and Gordon, S., "Thermodynamic Properties to 6000 K for 210 Substance Involving the First 18 Elements," NASA SP-3001, 1963.
23. Edward, D. K. and Menard, W. A., "Comparison of Models for Correlation of Total Band Absorptance," App. Optics, 3, 621, 1964.
24. Tiwari, S. N., "Radiative Interactions in Transient Energy Transfer in Gaseous Systems," Progress Report NAG-1-423, Dept. of Mechanical Engineering and Mechanics, Old Dominion University, Norfolk, VA, December 1985.
25. Smith, R. E. and Weigel, B. L., "Analytical and Approximate Boundary Fitted Coordinate System for Fluid Flow Simulation, AIAA Paper No. 80-0192, January 1980.
26. MacCormack, R. W., "The Effect of Viscosity in Hypersonic Impact Cratering," AIAA Paper No. 69-354, May 1969.
27. Wilkin, J. H., The Algebraic Eigenvalue Problem, Oxford University Press, Oxford, England, 1965, pp. 233-236.

28. Householder, A. S., The Theory of Matrices in Numerical Solution Analysis, Dover Publication, New York, 1964. pp. 122-140.
29. Tiwari, S. N. and Singh, D. J., "Interaction of Transient Radiation in Nongray Gaseous Systems," Progress Report NAG-1-423, Dept. of Mechanical Engineering and Mechanics, Old Dominion University, Norfolk, VA, January 1987.
30. Tiwari, S. N., Singh, D. J., and Kumar, A., "Transient Radiative Energy Transfer in Nongray Gases," AIAA Paper No. 87-0323, January 1987.

APPENDICES

APPENDIX A

DERIVATION OF CONDUCTION HEAT FLUX TERMS

To simplify the Eqs. (2.3) to Eqs. (2.4), the Lewis number is assumed to be unity. This simplification is carried out in detail for Eq. (2.3b) and the same is applied to Eq. (2.3a). Using the expressions for the thermal diffusivity (α) and Lewis number (L_e), Eq. (2.3b) can be expressed as

$$\alpha = K/\rho \bar{C}_p$$

$$L_e = \alpha/D$$

$$q_{cy} = -\rho D (L_e \bar{C}_p \frac{\partial T}{\partial y} + \sum_{i=1}^m \frac{\partial f_i}{\partial y} h_i) \quad (A.1)$$

Defining the binary diffusion coefficient D in terms of the Pandtl and Lewis number Eq. (A.1) can be expresses as

$$Pr = \nu/\alpha$$

$$D = \frac{\alpha}{L_e} = \frac{\nu/Pr}{L_e} = \frac{\mu}{\rho Pr L_e}$$

$$q_{cy} = -\frac{\mu}{Pr} [\bar{C}_p \frac{\partial T}{\partial y} + \sum_{i=1}^m \frac{\partial f_i}{\partial y} h_i] \quad (A.2)$$

where

$$\bar{C}_p = \sum_{i=1}^m f_i C_{p,i}$$

The static enthalpy of the mixture is given by the relation

$$h = \sum_{i=1}^m [h_i^0 + \int_0^T C_{p,i} d\eta] f_i \quad (A.3)$$

It should be noted that η is a dummy variable employed to evaluate the sensible enthalpy. Using the Leibnitz formula Eq. (A.3) is differentiated to obtain

$$\begin{aligned}\frac{\partial h}{\partial y} &= \sum_{i=1}^m \left[(h_i^0 + \int_0^T c_{p_i}(\eta) d\eta) \frac{\partial f_i}{\partial y} + f_i \frac{\partial h_i^0}{\partial y} \right. \\ &\quad \left. + f_i \int_0^T \frac{\partial c_{p_i}(\eta)}{\partial y} d\eta + f_i c_{p_i}(T) \frac{\partial T}{\partial y} \right] \quad (A.4)\end{aligned}$$

The coefficients of the first differential on the right side is equal to h_i and the second and third terms are identical to zero, therefore, Eq. (A.4) reduces to

$$\frac{\partial h}{\partial y} = \sum_{i=1}^m \left[h_i \frac{\partial f_i}{\partial y} + f_i c_{p_i} \frac{\partial T}{\partial y} \right]$$

or

$$\frac{\partial h}{\partial y} = \sum_{i=1}^m h_i \frac{\partial f_i}{\partial y} + c_p \frac{\partial T}{\partial y} \quad (A.5)$$

Substituting Eq. (A.5) into Eq. (A.2), q_{cy} is expressed as

$$q_{cy} = - \frac{\mu}{Pr} \frac{\partial h}{\partial y}$$

or

$$q_{cy} = - \frac{\gamma \mu}{Pr} \frac{\partial e}{\partial y}$$

APPENDIX B

EXPRESSIONS FOR RADIATIVE FLUX

The general equation of radiative flux is obtained from Ref. 5 as

$$\begin{aligned}
 q_{R\lambda}(\tau_\lambda) = & 2\pi \int_0^1 I_\lambda^+(0, \mu) e^{-\tau_\lambda/\mu} \mu d\mu - 2\pi \int_0^1 I_\lambda^-(\tau_{0\lambda}, -\mu) e^{-(\tau_{0\lambda}-\tau_\lambda)/\mu} \mu d\mu \\
 & + 2 \int_0^{\tau_\lambda} \left[\frac{\kappa_\lambda}{\beta_\lambda} e_{b\lambda}(t) + \frac{\gamma_\lambda}{4\beta_\lambda} G_\lambda(t) \right] E_2(\tau_\lambda - t) dt \\
 & - 2 \int_{\tau_\lambda}^{\tau_{0\lambda}} \left[\frac{\kappa_\lambda}{\beta_\lambda} e_{b\lambda}(t) + \frac{\gamma_\lambda}{4\beta_\lambda} G_\lambda(t) \right] E_2(t - \tau_\lambda) dt \quad (B.1)
 \end{aligned}$$

where the $E_n(t)$ are the exponential integral functions defined by

$$E_n(t) = \int_0^1 \mu^{n-2} e^{-t/\mu} d\mu$$

For a diffuse surface the quantities $I_\lambda^+(0, \mu)$ and $I_\lambda^-(\tau_{0\lambda}, \mu)$ are given as

$$2\pi \int_0^1 I_\lambda^+(0, \mu) e^{-\tau_\lambda/\mu} \mu d\mu = 2B_\mu E_3(\tau_\lambda) \quad (B.2)$$

$$2\pi \int_0^1 I_\lambda^-(\tau_{0\lambda}, -\mu) e^{-(\tau_{0\lambda}-\tau_\lambda)/\mu} \mu d\mu = 2B_{2\lambda} E_3(\tau_{0\lambda} - \tau_\lambda)$$

Substituting Eq. (B.2) into Eq. (B.1), and neglecting the scattering terms ($\gamma_\lambda = 0$, $\beta_\lambda = \kappa_\lambda + \gamma_\lambda$), there is obtained

$$\begin{aligned}
 q_{R\lambda}(\tau_\lambda) = & 2B_{1\lambda} E_3(\tau_\lambda) - 2B_{2\lambda} E_3(\tau_{0\lambda} - \tau_\lambda) \\
 & + 2 \int_0^{\tau_\lambda} e_{b\lambda}(t) E_2(\tau_\lambda - t) dt - 2 \int_{\tau_\lambda}^{\tau_{0\lambda}} e_{b\lambda}(t) E_2(t - \tau_\lambda) dt \quad (B.3)
 \end{aligned}$$

From the Appendix B of Ref. 5, one finds

$$\int E_n(t) dt = -E_{n+1}(t); \quad E_n(0) = \frac{1}{n-1} \quad (B.4)$$

Now, consider the first integral in Eq. (B.3)

$$I_1 = \int_0^{\tau_\lambda} E_2(\tau_\lambda - t) dt \quad (B.5)$$

By defining $y = \tau_\lambda - t$, $dy = -dt$, Eq. (B.5) is expressed as

$$\begin{aligned} I_1 &= \int_{\tau_\lambda}^0 E_2(y) (-dy) = \int_0^{\tau_\lambda} E_2(y) dy \\ &= -E_3(y) \Big|_0^{\tau_\lambda} = E_3(0) - E_3(\tau_\lambda) \end{aligned}$$

Thus

$$E_3(\tau_\lambda) = E_3(0) - I_1 = \frac{1}{2} - \int_0^{\tau_\lambda} E_2(\tau_\lambda - t) dt \quad (B.6)$$

The second integral in (B.3) is written as

$$I_2 = \int_{\tau_\lambda}^{\tau_{0\lambda}} E_2(t - \tau_\lambda) dt \quad (B.7)$$

By defining $y = t - \tau_\lambda$, Eq. (B.7) is written as

$$\begin{aligned} I_2 &= \int_0^{\tau_{0\lambda} - \tau_\lambda} E_2(y) dy = -E_3(y) \Big|_0^{\tau_{0\lambda} - \tau_\lambda} \\ &= -[E_3(\tau_{0\lambda} - \tau_\lambda) - E_3(0)] \end{aligned}$$

Thus,

$$E_3(\tau_{0\lambda} - \tau_\lambda) = E_3(0) - I_2 = \frac{1}{2} - \int_{\tau_\lambda}^{\tau_{0\lambda}} E_2(t - \tau_\lambda) dt \quad (B.8)$$

A substitution of Eqs. (B.6) and (B.8) into Eq. (B.3) results in

$$\begin{aligned}
 q_{R\lambda}(\tau_\lambda) = & e_{1\lambda} - e_{2\lambda} + 2 \left\{ \int_0^{\tau_\lambda} [e_{b\lambda}(t) - e_{1\lambda}] E_2(\tau_\lambda - t) dt \right. \\
 & \left. - \int_{\tau_\lambda}^{0\lambda} [e_{b\lambda}(t) - e_{2\lambda}] E_2(t - \tau_\lambda) dt \right\} \quad (B.9)
 \end{aligned}$$

Equation (B.9) is exactly like Eq. (3.9) if it is written in terms of the wave number (ω) instead of the wave length (λ).

APPENDIX C

BOUNDARY CONDITIONS FOR GRAY MODEL

The evaluation of the second order differential equation, Eq. (3.18), requires two boundary conditions. In this Appendix, the boundary conditions for nonblack diffuse surfaces are derived.

Applying the exponential kernal approximations to Eq. (3.8), one obtains

$$q_{R\lambda}(\tau_\lambda) = B_{1\lambda} e^{-\frac{3}{2}\tau_\lambda} - B_{2\lambda} e^{-\frac{3}{2}(\tau_{0\lambda}-\tau_\lambda)} + \frac{3}{2} \int_0^{\tau_\lambda} e_{b\lambda}(t) e^{-\frac{3}{2}(\tau_\lambda-t)} dt \\ - \frac{3}{2} \int_{\tau_\lambda}^{\tau_{0\lambda}} e_{b\lambda}(t) e^{-\frac{3}{2}(t-\tau_\lambda)} dt \quad (C.1)$$

By employing the Leibnitz formula, the divergence of the radiative flux is expressed as

$$\frac{dq_{R\lambda}(\tau_\lambda)}{d\tau_\lambda} = -\frac{3}{2} B_{1\lambda} e^{-\frac{3}{2}\tau_\lambda} - \frac{3}{2} B_{2\lambda} e^{-\frac{3}{2}(\tau_{0\lambda}-\tau_\lambda)} \\ - \frac{9}{4} \int_0^{\tau_\lambda} e_{b\lambda}(t) e^{-\frac{3}{2}(\tau_\lambda-t)} dt + \frac{3}{2} e_{b\lambda}(\tau_\lambda) \\ - \frac{9}{4} \int_{\tau_\lambda}^{\tau_{0\lambda}} e_{b\lambda}(t) e^{-\frac{3}{2}(t-\tau_\lambda)} dt + \frac{3}{2} e_{b\lambda}(\tau_\lambda) \quad (C.2)$$

Evaluating the radiative flux terms at the lower and upper walls the relations for $q_{R\lambda}$ and $\text{div}q_{R\lambda}$ are expressed as

$$q_{R\lambda}(0) = B_{1\lambda} - B_{2\lambda} e^{-\frac{3}{2}\tau_{0\lambda}} - \frac{3}{2} \int_0^{\tau_{0\lambda}} e_{b\lambda}(t) e^{-\frac{3}{2}t} dt \quad (C.3)$$

$$q_{R\lambda}(\tau_{0\lambda}) = B_{1\lambda} e^{-\frac{3}{2}\tau_{0\lambda}} - B_{2\lambda} + \frac{3}{2} \int_0^{\tau_{0\lambda}} e_{b\lambda}(t) e^{-\frac{3}{2}(\tau_{0\lambda}-t)} dt \quad (C.4)$$

$$\left. \frac{dq_{R\lambda}(\tau_\lambda)}{d\tau_\lambda} \right|_{\tau_\lambda=0} = -\frac{3}{2} B_{1\lambda} - \frac{3}{2} B_{2\lambda} e^{-\frac{3}{2}\tau_{0\lambda}} - \frac{9}{4} \int_0^{\tau_{0\lambda}} e_{b\lambda}(t) e^{-\frac{3}{2}t} dt + 3 e_{b\lambda}(0) \quad (C.5)$$

$$\begin{aligned} \left. \frac{dq_R(\tau_\lambda)}{d\tau_\lambda} \right|_{\tau_\lambda=\tau_{0\lambda}} &= -\frac{3}{2} B_{1\lambda} e^{-\frac{3}{2}\tau_{0\lambda}} - \frac{3}{2} B_{2\lambda} - \frac{9}{4} \int_0^{\tau_{0\lambda}} e_{b\lambda}(t) e^{-\frac{3}{2}(\tau_{0\lambda}-t)} \\ &\quad + 3 e_{b\lambda}(\tau_{0\lambda}) \end{aligned} \quad (C.6)$$

Multiplying Eq. (C.3) by $\frac{3}{2}$ and Eq. (C.4) by $(-\frac{3}{2})$ and then substituting into Eqs. (C.5) and (C.6) respectively, one obtains

$$-\left. \frac{dq_{R\lambda}}{d\tau_\lambda} \right|_{\tau_\lambda=0} + \frac{3}{2} q_{R\lambda}(0) = 3 B_{1\lambda} - 3 e_{b\lambda}(0) \quad (C.7)$$

$$\left. \frac{dq_{R\lambda}}{d\tau_\lambda} \right|_{\tau_\lambda=\tau_{0\lambda}} + \frac{3}{2} q_{R\lambda}(\tau_{0\lambda}) = 3 e_{b\lambda}(\tau_{0\lambda}) + 3 B_{2\lambda} \quad (C.8)$$

The radiosities $B_{1\lambda}$ and $B_{2\lambda}$ are expressed as

$$B_{1\lambda} = \varepsilon_{1\lambda} e_{b1\lambda} + (1 - \varepsilon_{1\lambda}) [B_{1\lambda} - q_{R\lambda}(0)] \quad (C.9a)$$

$$B_{2\lambda} = \varepsilon_{2\lambda} e_{b2\lambda} + (1 - \varepsilon_{2\lambda}) [B_{2\lambda} - q_{R\lambda}(\tau_{0\lambda})] \quad (C.9b)$$

Rearranging Eqs. (C.9) and substituting for $B_{1\lambda}$ and $B_{2\lambda}$ into Eqs. (C.7) and (C.8) the boundary conditions are expressed as

$$\left(\frac{1}{\varepsilon_{1\lambda}} - \frac{1}{2} \right) q_{R\lambda}(0) - \frac{1}{3} \left. \frac{dq_{R\lambda}}{d\tau_\lambda} \right|_{\tau_\lambda=0} = e_{b1\lambda} - e_{b\lambda}(0) \quad (C.10a)$$

$$\left(\frac{1}{\epsilon_{2\lambda}} - \frac{1}{2}\right) q_{R\lambda}(\tau_{0\lambda}) + \frac{1}{3} \left.\frac{dq_{R\lambda}}{d\tau_\lambda}\right|_{\tau_\lambda=\tau_{0\lambda}} = e_{b\lambda}(\tau_{0\lambda}) - e_{b2\lambda} \quad (C.10b)$$

For the gray medium, λ dependence is deleted; and then Eqs. (C.10) are exactly like Eqs. (3.19).